

Article

Photocatalytic Filtration of Zinc Oxide-Based Membrane with Enhanced Visible Light Responsiveness for Ibuprofen Removal

Nurafiqah Rosman ¹, Wan Norharyati Wan Salleh ^{1,*}, Juhana Jaafar ¹, Zawati Harun ², Farhana Aziz ¹ and Ahmad Fauzi Ismail ¹

¹ Advanced Membrane Technology Research Centre (AMTEC), School of Chemical and Energy Engineering, Universiti Teknologi Malaysia, Skudai 81310, Johor, Malaysia; afaqhrosman@gmail.com (N.R.); juhana@petroleum.utm.my (J.J.); farhana@petroleum.utm.my (F.A.); afauzi@utm.my (A.F.I.)

² Integrated Material and Process, Advanced Materials and Manufacturing Centre (AMMC), Faculty of Mechanical and Manufacturing Engineering, Universiti Tun Hussein Onn Malaysia, Parit Raja, Batu Pahat 86400, Johor, Malaysia; zawati@uthm.edu.my

* Correspondence: hayati@petroleum.utm.my

Abstract: The growing interest in mixed matrix membranes (MMMs) for developing photocatalytic membranes has provided a new direction in the search for efficient methods to concurrently separate and degrade contaminants. In this study, a visible light-responsive photocatalyst was blended into a polyvinylidene fluoride (PVDF) membrane casting solution to prepare PVDF-ZnO/Ag₂CO₃/Ag₂O MMMs using the wet phase inversion method. The potential of ZnO/Ag₂CO₃/Ag₂O as a photocatalytic component that is incorporated into the membrane was explored in detail under various loadings (0.5–2.91 wt%). The membranes were tested under ibuprofen (IBF) aqueous solution to analyze the membrane behavior in the synergistic combination of membrane filtration and photodegradation. The resulting PVDF-ZnO/Ag₂CO₃/Ag₂O membrane with a rougher membrane surface area and excellent light harvesting capability showed higher photocatalytic filtration activity in removing IBF under visible light irradiations. The MMM fluxes demonstrated higher IBF fluxes than their initial fluxes at certain durations. This indicates that the membrane actively responds to light irradiation. The increase in the positive flux could be attributed to the photoinduced hydrophilicity generated by the ZnO/Ag₂CO₃/Ag₂O photocatalyst, resulting in easier water layer formation and rapid transport through membranes. The highest IBF removal was demonstrated by the PVDF-ZAA₂ membrane (1.96 wt% loading), with 49.96% of IBF removal within 180 min upon visible light irradiation. The reason for this lower IBF removal is that the UF membrane pores exceed the size of IBF molecules, thereby preventing the size exclusion mechanism. Thus, charge repulsion, hydrophobic adsorption, and photocatalytic activity were considered along with the IBF removal of the photocatalytic membranes. However, the recyclability of the PVDF-ZAA₂ photocatalytic membrane showed a great improvement, with 99.01% of IBF removal recovery after three cycles. These results highlight the potential of such hybrid membranes in mitigating membrane fouling by providing a platform for photocatalysts to continuously degrade pollutants present in such wastewaters. Therefore, the hybridization of a photocatalyst and membrane provides insight that could be utilized to improve and retrofit current water effluent treatment methods.

Keywords: photocatalyst; ultrafiltration; mixed matrix membrane; pharmaceutical; antifouling



Citation: Rosman, N.; Wan Salleh, W.N.; Jaafar, J.; Harun, Z.; Aziz, F.; Ismail, A.F. Photocatalytic Filtration of Zinc Oxide-Based Membrane with Enhanced Visible Light Responsiveness for Ibuprofen Removal. *Catalysts* **2022**, *12*, 209. <https://doi.org/10.3390/catal12020209>

Academic Editor: Vincenzo Vaiano

Received: 18 December 2021

Accepted: 27 January 2022

Published: 10 February 2022

Publisher's Note: MDPI stays neutral with regard to jurisdictional claims in published maps and institutional affiliations.



Copyright: © 2022 by the authors. Licensee MDPI, Basel, Switzerland. This article is an open access article distributed under the terms and conditions of the Creative Commons Attribution (CC BY) license (<https://creativecommons.org/licenses/by/4.0/>).

1. Introduction

In recent decades, emerging contaminants found in aqueous streams, such as hormones, pesticides, pharmaceuticals, and personal care products, have received widespread public attention because of their adverse effects on human health, plants, soils, and aquatic systems [1,2]. A number of studies have demonstrated the persistence of their toxicological effects, even at low concentrations of nanograms per liter; these contaminants become

more complex when they are mixed [3,4]. The compounds in this class are mostly found in prescription medicines, over-the-counter therapeutic drugs, cosmetics, plastic additives, and other industrial products [5]. In conjunction with the rapid growth of the population and industrialization, the demand for these products also rises, which results in an increased level of contaminants in water sources due to improper treatment and disposal of municipal and industrial effluent (Rudd et al., 2016).

Pharmaceutical residues have been identified as a growing issue among emerging contaminants in many water quality studies. A non-steroidal anti-inflammatory drug (NSAID) called ibuprofen (IBF) has become the second most consumed drug in the world, belonging to the class of compounds with carboxylic aryl acids that provide acidic effects (Georgaki et al., 2014). According to toxicology studies, long-term exposure to such compounds could cause kidney failure and stomach injuries in humans (Hu et al., 2013). It was reported that IBF has been found in hospital wastewater [6], sewage treatment [7], plant effluents [8], soil [9], and seawater [10]. Consequently, the removal of pharmaceuticals from the environment becomes crucial. A wide variety of conventional methods for wastewater treatment, including adsorption, coagulation, biological treatment, and activated sludge, cannot fully remove the persistent, nonbiodegradable chemicals [11]. The water must, therefore, be treated several times in order to remove IBF and its derivatives before it is discharged, for example, by introducing a membrane technology at the polishing stage.

Recently, research activity and extensive scientific investigation on integration or hybrid membrane and photocatalytic materials has aroused great attention in the last few years. In general, photocatalytic materials are subjected to the formation and utilization of a powerful oxidant called the hydroxyl radical ($\bullet\text{OH}$) [12]. The strong oxidant produced from photocatalysis can be beneficial in eliminating membrane fouling and remediation of pharmaceutical compounds via the oxidation of the foulant and enhancement of the permeability performance of the membrane. Recently, Tran et al. [13] showed that the immobilization of TiO_2 in PVDF polymer membrane induced the membrane's surface to become more hydrophilic upon ultraviolet (UV) irradiation. The flux behavior of the membrane's pure water flux rises significantly when UV is activated during filtration, depending on irradiance and UV cycle length effect. In this regard, the photocatalyst can play a key role due to its ability to minimize membrane fouling and maintain membrane performance throughout the process [14]. The integration of both technologies will allow the decomposition of the retained pollutants via photocatalysis, which is conducive to alleviating membrane fouling [15]. Lee et al. reported that photocatalytic membranes comprised of N- TiO_2 membranes create multifunctional inorganic membranes capable of destroying pollutants and self-cleaning under solar irradiation [16]. Therefore, the hybridization of these processes could offer the dual functionality of separating pollutants from water and destroying the pollutants concurrently via oxidative processes, which is an attractive alternative.

However, most common photocatalyst semiconductors, for instance, TiO_2 and ZnO , have a band gap larger than 3.1 eV, which limits its application in the visible light region ($\lambda \geq 387$ nm). Hence, modifying and developing photocatalysts with other appropriate materials that have good light response, charge separation ability, and high photocatalytic stability under visible light is beneficial for the modification of TiO_2 and ZnO into the light absorption spectrum of a lower energy region (i.e., visible light) [17]. Heterojunction is one of the methods that could uplift the photocatalyst's performance by providing an efficient electron-hole generation for photodegradation processes [18]. In fact, currently, the ternary heterojunction photocatalyst is seen as an effective photocatalyst for mineralization, including pharmaceutical compounds. Plenty of evidence suggests that ternary heterojunction with enhanced physicochemical characteristics forces a quick transfer of photoexcited electrons from a semiconductor to other adjoining semiconductors in cascade form, hence, quickening the separation of e^-/h^+ pairs and enhancing the photocatalytic efficacy. For instance, a facile method comprised of in situ calcination and a photochemical reduction self-assembly process was used by Yang et al. [19] for the fabrication of ternary

NaTaO₃/g-C₃N₄/graphene oxide nanocomposites with various NaTaO₃ compositions for the photodegradation of RhB in aqueous solution. The kinetic studies on the degradation activity of the samples revealed that NaTaO₃/g-C₃N₄/graphene oxide nanocomposites exhibited the highest photocatalytic activity, which is 3.1 times faster than that of pure g-C₃N₄ and 2.1 times faster than NaTaO₃/g-C₃N₄. Recently, Liang et al. [20] synthesized a porous loofah sponge-like ternary heterojunction g-C₃N₄/Bi₂WO₆/MoS₂ nanocomposite. The as-prepared Ag₃PO₄/ZnFe₂O₄/ZnO porous photocatalyst represented excellent photoactivity for sulfamethoxazole (SMX) removal under visible light irradiation with over 99% within 60 min. The fitted pseudo-first-order kinetic rate constant of the ternary photocatalyst reached 0.089 min⁻¹, which was 3.17 times than that of pure g-C₃N₄. Hence, ternary heterojunctions have established much interest over the corresponding binary nanocomposite and pure semiconductor photocatalyst due to the cooperative features of the three constituents and their conceivable contribution to enhanced photocatalytic activity.

Basically, the integration of both technologies in the form of a membrane can be simplified with a mixed matrix membrane (MMM) through the blending method because of its simplicity and inexpensiveness [21,22]. In fact, the incorporation of a heterojunction photocatalyst into a polymer membrane is barely reported on; hence, in this study, the embedment of ZnO/Ag₂CO₃/Ag₂O into a PVDF polymer as an MMM could be a new branch of knowledge on how the membrane can potentially improve photocatalytic filtration, as well as the membrane antifouling behavior. As far as the subject is concerned, the studies investigating the photocatalytic filtration behavior of ternary photocatalysts in a polymer membrane towards IBF solution, especially under visible light irradiation, are scarce.

2. Result and Discussion

2.1. Characterization of ZnO/Ag₂CO₃/Ag₂O Photocatalyst

The ZnO/Ag₂CO₃/Ag₂O was characterized for its phase structure, crystallinity, and optical properties, as shown in Figure S1. An extensive discussion of the characteristics of the ZnO/Ag₂CO₃/Ag₂O photocatalyst can be found in our previous study [23]. In brief, the synthesis of the ZnO/Ag₂CO₃/Ag₂O photocatalyst via co-precipitation and the low temperature calcination method allowed the heterojunction of Ag₂CO₃ on ZnO, followed by the in-situ phase transformation of Ag₂CO₃ to Ag₂O. This phase transformation led to the presence of a mixed phase Ag₂CO₃/Ag₂O over ZnO surfaces, as observed in Figure S1a. The grain boundary contained a mixture of Ag₂CO₃, Ag₂O, and ZnO grains that inhibited electron-hole recombination between them. Further analysis of the TEM images using GATAN Microscopy Suite 2.1 (AMETEK Pleasanton, California, United States) revealed that the d-spacing for crystal plane (101) corresponded to 0.2448 nm for ZnO, 0.2666 nm for crystal plane (130) of Ag₂CO₃, and 0.2773 nm for crystal plane (111) of Ag₂O. In this regard, the SAED pattern of the photocatalyst in Figure S1b displayed multiple bright spot rings, demonstrating the crystalline structure of the ZnO/Ag₂CO₃/Ag₂O photocatalyst. The crystal planes of ZnO, Ag₂CO₃, and Ag₂O that react with different bright dot circles were in accordance with the d-spacing of the XRD results in Figure S1c. The characteristic peaks of 36.25°, 34.87°, and 32.79° on the crystal plane of ZnO (101), Ag₂CO₃ (130) and Ag₂O (111), respectively, indicate that the ZnO/Ag₂CO₃/Ag₂O photocatalyst was successfully synthesized. Figure S1d shows the band gap characteristics of the pristine ZnO, binary, and ternary heterojunction photocatalyst. It was found that the ternary ZnO/Ag₂CO₃/Ag₂O photocatalyst exhibits the narrowest band gap (2.86 eV), which is advantageous for visible light harvesting. As a result of the synergistic effects of Ag₂CO₃/Ag₂O heterostructures over ZnO, the heterostructures provided a good electron/hole separation that enabled effective photocatalysis.

2.2. Membrane Morphology and Structure

Figure 1 shows the evaluation of the morphic structure of the prepared membrane. The SEM images of the cross-sectional and inner structures of pristine PVDF membrane and MMMs clearly illustrate that all of the membranes exhibit a typical asymmetric structure,

which consists of a skin layer and microvoid sublayer. Basically, a skin layer (top layer) is relatively dense and thin, which constitutes the selective and active surface of the membrane. It is supported by a macrovoid structure resulting from a non-solvent and solvent exchange process all the way through from the top surface to the bottom of the membrane during phase separation [24].

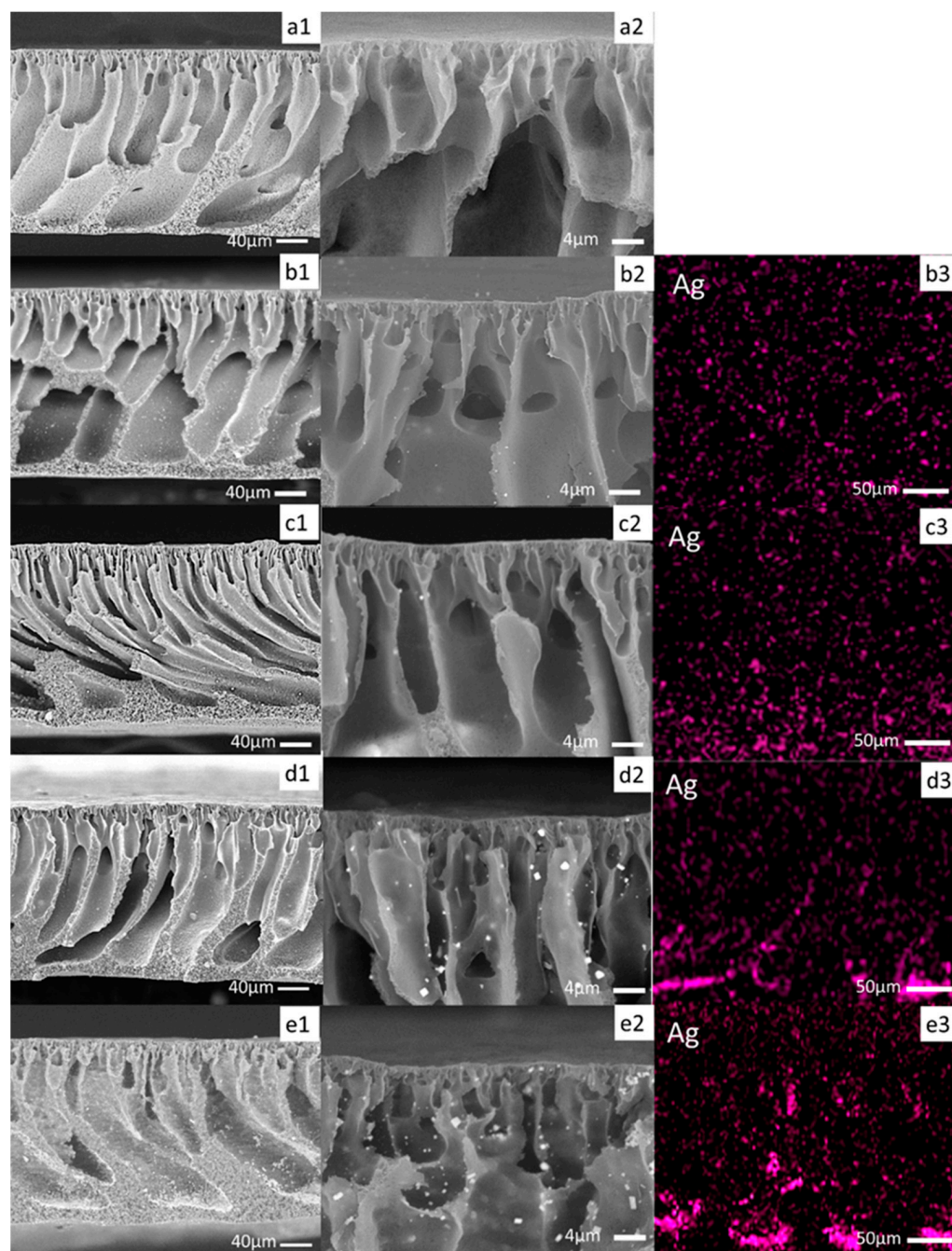


Figure 1. The SEM images of the cross-sectional view of the pristine PVDF and PVDF-ZAA_x (x:0.5–3) (a–e); its high magnification of the membrane top layer (a1–e1); and EDX mapping for Ag element distribution across the MMMs' structure (b2–e2).

The addition of 0.5 wt% ZnO/Ag₂CO₃/Ag₂O in PVDF membrane increased the number of pore structures (as seen in Figure 1b1) at the top layer of the membrane. The addition of the photocatalyst in the casting solution caused a faster exchange rate over the membrane surfaces during the phase inversion process, thus leading to the increase in small formations at the top layer. A similar phenomenon was also observed in several

previous works, where the increasing hydrophilicity of particles attracted more water inside the membrane surface, resulting in an increase of small finger-like pores [25,26]. It can be observed that there was an increase in the density of pores at the sublayer of the membrane compared with that in the pristine PVDF (Figure 1b).

When 0.99 wt% of ZnO/Ag₂CO₃/Ag₂O was added, a decreased pore density was observed at the membrane sublayer when compared with the pristine PVDF (Figure 1b). The hydrophilic nature of ZnO/Ag₂CO₃/Ag₂O, as discussed in previous research [23], induced a higher water penetration and solvent departure across the membrane, which seemed to favor the finger-like macrovoid structure [27]. Moreover, as suggested by Sotito et al. [28], it could also be due to interfacial stress between the polymer and nanoparticles, which led to the formation of pores that reflected polymer phase shrinking during the demixing process. In contrast, the incorporation of ZnO/Ag₂CO₃/Ag₂O at a higher loading (1.96 and 2.91 wt%) led to a larger macrovoid sublayer with a smaller pore density remaining underneath the membrane skin layer. It is a well-established fact that for higher concentrations, the viscosity of the membrane dope will continue to increase. The increase of viscosity leads to a slower rate of mass transfer diffusion between the solvent and water during the phase inversion, which indirectly induces delay demixing. [29,30]. Even with slower water penetration throughout the membrane, the hydrophilic nature of ZnO/Ag₂CO₃/Ag₂O allows water to diffuse inside the polymer matrix, forming larger macrovoids at the bottom of the membrane. In fact, it was supported with SEM–EDX images on photocatalyst distribution in Figure 1e3, where the precipitated hydrophilic photocatalyst allows for larger microvoid at the bottom of the membrane.

Furthermore, to confirm the photocatalyst distribution of ZnO/Ag₂CO₃/Ag₂O in the PVDF-ZAA MMMs, EDX mapping was employed on the cross-section micrograph in Figure 1b3–e3. The EDX profile of silver (Ag) presented that the photocatalyst was well dispersed throughout the PVDF matrix without agglomeration in 0.5 wt%. There is a possibility that the presence of ZnO/Ag₂CO₃/Ag₂O had only slightly modified the viscosity of the casting solution [27]. Hence, formation of macrovoids is almost similar in comparison to the pristine PVDF membrane, except on the membrane skin layer, as observed in Figure 1b2. As the 0.99 wt% of ZnO/Ag₂CO₃/Ag₂O was added, it tended to slightly precipitate at the bottom layer of the membrane, beginning to be agglomerated. Meanwhile, at higher loading (1.96 and 2.91 wt%), an obvious agglomeration was seen, with apparent precipitation of the particles at the bottom of the membrane. This precipitation could also be due to the excess of particles in the membrane, as well as coming from the effect of gravity upon the evaporation procedure (30 s) in the membrane casting process.

Detailed elements of the MMMs are tabulated in Table 1. According to result, the oxygen (O), zinc (Zn), and silver (Ag) elements were logically increased with increased photocatalyst loading. On the contrary, the fluoride (F) and carbon (C) elements were found to have decreased with increasing photocatalyst loading. This situation could be attributable to the photocatalyst loading in the PVDF polymer matrix, which lowered the mass of the F element. Overall, the results presented in Table 1 are in accordance with the work by Liu et al. [31].

Table 1. Characteristics of prepared membrane based on elemental composition.

Peak Assignment	Map Sum Spectrum (wt%)			
	PVDF-ZAA _{0.5}	PVDF-ZAA ₁	PVDF-ZAA ₂	PVDF-ZAA ₃
Fluoride (F)	55.3	54.6	53.3	51.4
Carbon (C)	42.6	41.3	40.4	59.2
Oxygen (O)	1.3	1.5	2.5	3.9
Zinc (Zn)	0.5	1.4	2.3	3.7
Silver (Ag)	0.3	1.3	1.6	1.8

The membrane morphology was further evaluated in Figure 2, which shows the 3D AFM surface images of all membranes prepared with different photocatalysts with a scan size of 10 μm × 10 μm. The surface morphologies of the membranes were strongly

influenced by the incorporation of photocatalyst loading. In these images, the light area represents higher membrane surface, while the dark regions represent valley or membrane pores. All of the 3D AFM images exhibited nodule-like structures that aggregated on the membrane surfaces.

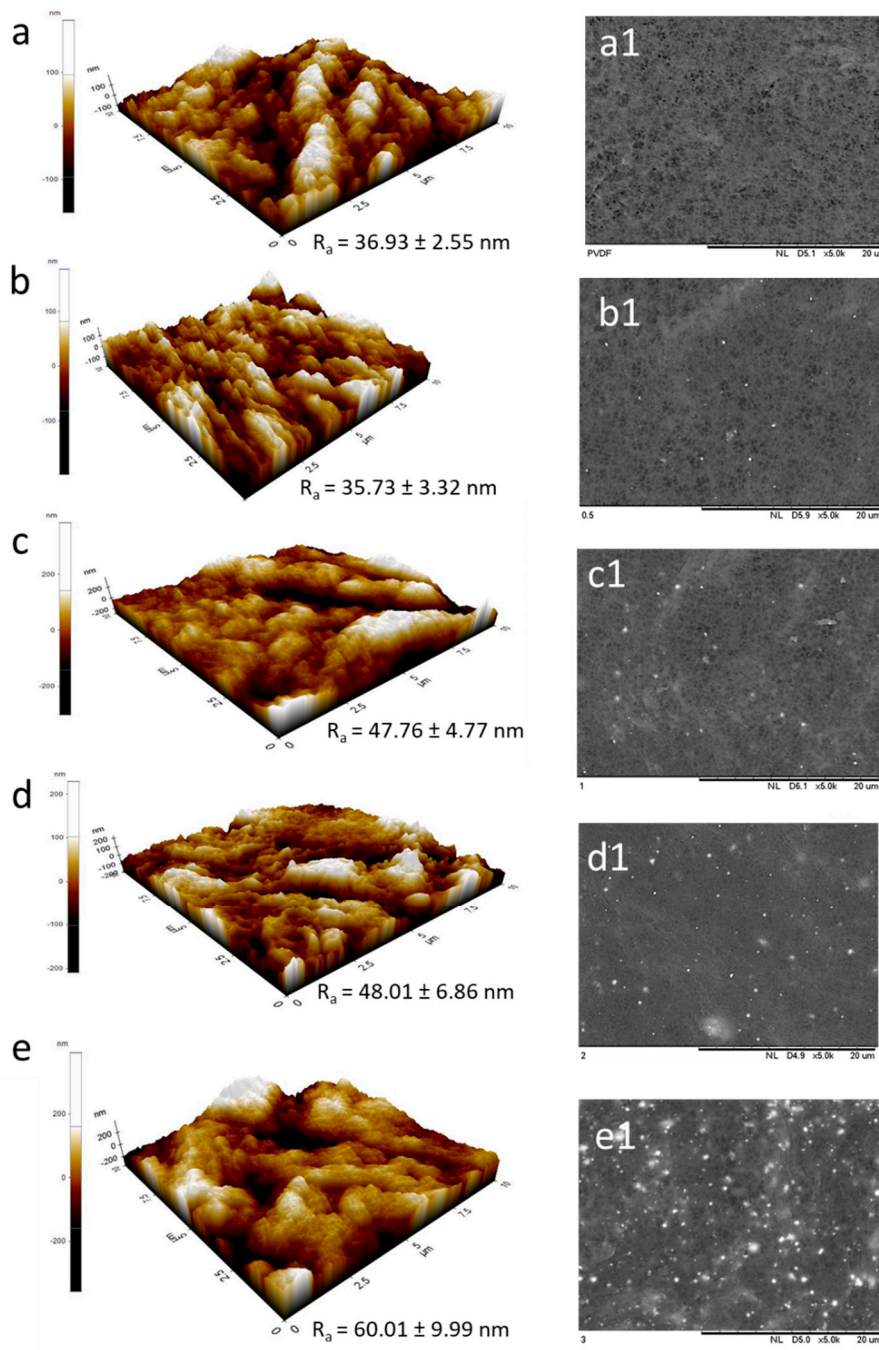


Figure 2. Three-dimensional (a–e) AFM surface images of PVDF and PVDF MMMs; (a1–e1) SEM images of membrane surface.

These surface roughness parameters of the membranes can be expressed in roughness (R_a), the root mean square of the Z data (R_q), and the mean difference between the highest peaks and lowest valleys (R_z), which are presented in Table 2. The roughness parameters for the membranes increased with increased ZnO/Ag₂CO₃/Ag₂O concentration in the PVDF polymer matrix, except for PVDF-ZAA_{0.5}. A slight decrease in the surface roughness of PVDF-ZAA_{0.5} can be explained by the exhibition of closely tight tiny pores over the

membrane skin layer. The roughness parameters of the Z-value (Rz), which is the vertical distance, are deep depressions (pores) and high peaks (nodules), illustrating a similar result where it gradually increased as the catalyst loading increased [32], except for PVDF-ZAA_{0.5}.

Table 2. AFM surface roughness values of the prepared membrane.

Membranes	Ra (Mean Surface Roughness) nm	Rq (Root Mean Square Roughness) nm	Rz (Difference between High Peak and Low Valley) nm
PVDF	36.930 ± 2.551	49.957 ± 1.858	463.866 ± 161.025
PVDF-ZAA _{0.5}	35.726 ± 3.323	45.057 ± 4.538	382.682 ± 35.404
PVDF-ZAA ₁	47.763 ± 4.767	61.203 ± 8.012	520.012 ± 89.788
PVDF-ZAA ₂	48.013 ± 6.858	59.815 ± 7.543	440.444 ± 18.170
PVDF-ZAA ₃	60.012 ± 9.99	77.525 ± 13.314	611.874 ± 138.050

The roughness value of the membrane surface, derived by AFM software, also included the pores and nodules on the membrane surface. Based on the SEM images in Figure 2, visible pores can be observed over the membrane surface and their maximum pore size is exhibited lower than 1 µm, which resembles the range of ultrafiltration membranes. Both the AFM and SEM images of the membrane surfaces show that as the photocatalyst deposition in the membrane increases, the pores in the membrane reduce due to the photocatalyst filling up the pores, decreasing the membrane porosity. Contrary to this, the filled pores do not smooth the membrane's surfaces. Based on Figures 1 and 2 of the SEM images, at higher photocatalyst loading (≥ 1.96 wt%), the membrane obviously suffers from agglomeration of ZnO/Ag₂CO₃/Ag₂O photocatalyst, either in the cross-section of the membrane or on its surface. It is therefore possible that the Ra, Rz, and Rq values of the PVDF-ZAA₂ and PVDF-ZAA₃ membranes were greater than those of the PVDF-ZAA_{0.5} and PVDF-ZAA₁ membranes. However, surfaces with a greater surface roughness are more beneficial to the photodegradation process [29]. Compared to smooth membrane surfaces, rough membrane surfaces significantly enhanced the amount of active catalyst surface area that was exposed to light irradiation in the ZnO/Ag₂CO₃/Ag₂O photocatalysts. In fact, the roughness of the membrane could trap more photons to undergo photocatalytic activity due to higher levels of photon absorption.

2.3. Membrane Wettability and Porosity

One of the significant features of the membranes that severely impacted the flux in terms of antifouling ability was surface hydrophilicity. This is generally measured based on the sessile drop method in which water is dropped onto the membrane's surface to measure the affinity of water to wet the membrane surface, wherein a decrease in angle suggests an increase in hydrophilicity. Figure 3 shows the contact angle results of various membranes as a function of time (s). Pristine PVDF membranes possessed the highest water contact angle values, while the membranes incorporated with the ZnO/Ag₂CO₃/Ag₂O tended to have decreased water contact angles as a function of time (s). The rate of water penetration over the membrane surface clearly indicates that PVDF-ZAA_{0.5} and PVDF-ZAA₁ possessed a high hydrophilicity rate, at 0.092 and 0.085°·s⁻¹, respectively. In fact, the water uptake and porosity also increased, which lowered the contact angle. The presence of hydroxyl functional groups in ZnO/Ag₂CO₃/Ag₂O, as discussed previously [26], provided a higher hydrogen bond over the membrane surfaces, which increased its water affinity properties [25]. Hence, the presence of hydrogen bonds bound the water droplet together and indirectly reduced the water surface tension, thus lowering the contact angle of the water droplet [33]. In terms of membrane fabrication, a homogeneously blended hydrophilic photocatalyst also triggered a decreased energy interface in the casting solution, resulting in instantaneously transported water during the phase inversion process on the top layer of the fabricated membranes [34]. This could also be the reason for the occurrence of closely tight pores over the membrane top layer (skin layer), as discussed in SEM images. In fact, at lower photocatalyst loadings (0.5 and 0.99 wt%), homogeneously photocatalyst distribution in the membrane allows for higher membrane porosity and membrane water uptake.

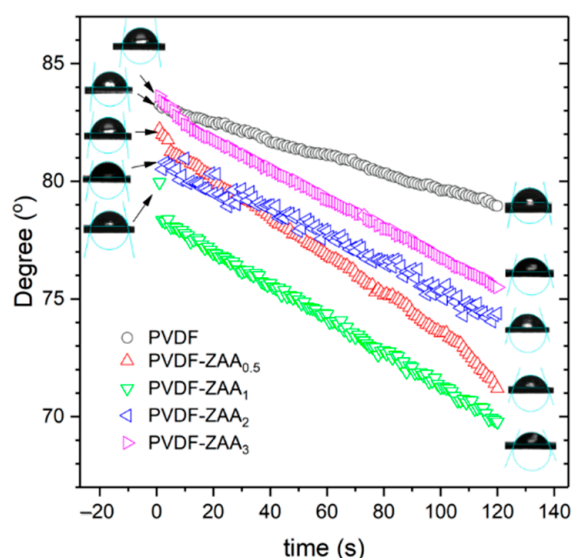


Figure 3. Dynamic contact angle of the prepared membranes.

Taking the whole figure into consideration, the porosity result in Table 3 strongly correlates with the morphological structure of the membrane, as illustrated in Figure 1. Membranes with lower photocatalyst loadings (0.5 and 0.99 wt%) exhibited higher porosity due to the homogenous distribution of photocatalysts within the polymer matrix, which resulted in faster solvent–non-solvent exchange during membrane formation. It was found that this faster rate of exchange was due to the presence of hydrophilic properties in the photocatalysts that allowed water to penetrate into the membrane during the inversion phase. In this situation, the reaction led to an increase in the membrane’s porosity. Similar results were obtained by Zhang et al. [35], where the porosity increased as the content of ZnO increased. As the photocatalyst loading increases (1.96 and 2.91 wt%), the porosity of the membranes tends to decrease. The increase in photocatalyst loading led the polymer dope viscosity to increase, resulting in a slower rate of mass transfer diffusion between the solvent and non-solvent (water) during the phase inversion, causing the delay demixing process. Although the presence of the ZnO/Ag₂CO₃/Ag₂O photocatalyst should increase the membrane porosity due to its hydrophilic nature, the excess amount will densify the membrane and fill the membrane pores [36].

Table 3. Water uptake and overall porosity determined by the gravimetric method.

Membrane	Water Uptake (g)	Porosity (%)	Contact Angle (° s ⁻¹)
PVDF	0.420 ± 0.0063	43.83	0.036
PVDF-ZAA _{0.5}	0.463 ± 0.0037	54.99	0.092
PVDF-ZAA ₁	0.450 ± 0.0987	58.55	0.085
PVDF-ZAA ₂	0.325 ± 0.0737	48.24	0.051
PVDF-ZAA ₃	0.221 ± 0.0049	45.52	0.068

Apart from that, the contact angle could also be influenced by the surface roughness of the membranes. As the amount of photocatalyst loading (1.96 wt% and 2.91 wt%) was continuously increased, both still exhibited a higher hydrophilicity with higher average surface roughness, as referred to in Figure 3. This unevenness of the membrane surface implies an enlargement of the effective membrane surface area, which increases hydrophilicity [37]. It has been reported that contact angles on rough solids are greater than on relatively smooth surfaces [38]. However, the water absorption rate on PVDF-ZAA₂ and PVDF-ZAA₃ showed a slight decrease in hydrophilicity than in PVDF-ZAA_{0.5} and PVDF-ZAA₁, followed by the membrane water uptake and membrane porosity. Similar observations by Yu et al. [39] accredited this situation to particle aggregation, which is less effective in terms of hydrophilic area and hydroxyl group number. In fact, the reduction of

pore size over the membrane's top layer influenced the rate of water absorption through the membrane.

2.4. Membrane Surface Charge

Membrane surface charge is a substantial parameter to study the membrane surface charge characteristic, as it affects the electrostatic interaction between the membranes and contaminant [40]. The zeta potential of the MMMs, evaluated from the streaming potential and streaming current measurements, is shown in Figure 4. The zeta potential varied with increased photocatalyst loading in the PVDF matrix owing to the position of ZnO/Ag₂CO₃/Ag₂O in the zeta potential, which was -6.04 ± 0.833 mV. Consequently, this meant that the membranes were slightly negatively charged after the ZnO/Ag₂CO₃/Ag₂O was incorporated. According to the results, the zeta potential values at approximately pH 7 were -33.3 mV for PVDF-ZAA_{0.5}, -32 mV for PVDF-ZAA₁, -34.6 mV for PVDF-ZAA₂, and -30 mV for PVDF-ZAA₃. All of the MMMs showed a negative zeta potential, therefore resulting in charge repulsion behavior for every membrane at an approximately similar neutral pH. The negative values of the zeta potential led to a decrease in the adhesion of negatively charged foulants (IBF) to the membrane surface, resulting in less fouling of the membrane. However, it would be difficult for a photocatalytic reaction to occur, whereby the negatively charge pollutant is repelled away from the membrane surface [41]. In this regard, the incorporation of ZnO/Ag₂CO₃/Ag₂O photocatalysts into the PVDF matrix does not alter the negatively charged surface of the PVDF, which characteristically leads to electrostatic repulsion between the membrane and the IBF pollutant. Therefore, it is expected that MMMs might be able to reduce membrane fouling, and this will be discussed further in the membrane performance analysis.

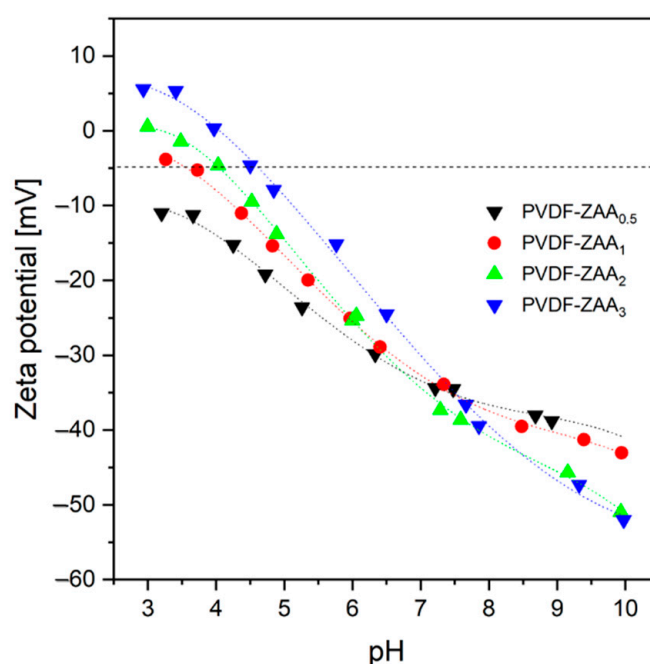


Figure 4. The surface zeta potential of MMMs as a function of pH.

2.5. The IBF Flux Properties of MMMs for Photocatalytic Filtration Performance

From Figure 5a, the MMMs were first tested in dark conditions. The PVDF-ZAA₁ portrayed the highest IBF permeation after 180 min with $32.27 \text{ L}\cdot\text{m}^{-2}\cdot\text{h}^{-1}$ in the dark conditions. It was followed by PVDF-ZAA_{0.5} and pristine PVDF at about 26.15 and $21.52 \text{ L}\cdot\text{m}^{-2}\cdot\text{h}^{-1}$, respectively. The improvement in IBF permeation for PVDF-ZAA_{0.5} and PVDF-ZAA₁ membranes is attributed to the hydrophilic interactions between the membranes and water, which enhances the passage of water through the membrane [42]. However, the IBF permeation of MMMs drops as the incorporation of the ZnO/Ag₂CO₃/Ag₂O catalyst continues. Meanwhile,

PVDF-ZAA₂ and PVDF-ZAA₃ are found to suffer in IBF permeation, with only 13.06 and 3.48 L·m⁻²·h⁻¹, respectively. The IBF flux rates in the dark were thus in the order of: PVDF-ZAA₁ > PVDF-ZAA_{0.5} > PVDF > PVDF-ZAA₂ > PVDF-ZAA₃. The flux trend was further analyzed in terms of relative flux, which is defined as the current permeate flux divided by the initial flux permeation of the membrane. Figure 5b shows that the relative flux gradually decreased over 180 min of filtration. These trends show similar behavior regardless of the different photocatalyst loading. PVDF-ZAA₂ and PVDF-ZAA₃ possessed the worst flux loss at approximately 0.7, while PVDF-ZAA_{0.5} showed the least flux loss at approximately 0.8. This result indicates that at a higher loading of ZnO/Ag₂O/Ag₂CO₃ (at 1.96 and 2.91 wt%), a higher fouling occurred compared with that in the pristine PVDF. As previously mentioned, the loading amount of ZnO/Ag₂O/Ag₂CO₃ strongly affects the permeate flux decline due to the morphological response upon nanoparticle incorporation. The excess loading led the distance between the particles to become too narrow, triggering them to aggregate; thus, homogenous dispersion can hardly be achieved. Additionally, such aggregation led to a decrease in pore size or clogging of the membrane pores [43], resulting in a less porous membrane and lower flux rate [44]. In addition, both flux losses could be influenced by the unevenness and rougher membrane surface, which, in turn, entrapped the IBF and plugged the membrane pore. Yet, both membranes were not in a serious flux decline, whereby the difference was only approximately 0.1 of flux ratio due to negatively charged MMMs at pH 7. As the pK_a value of IBF came to 4.50, IBF tends to deprotonate, resulting in negatively charged IBF. Therefore, the electrostatic repulsion mechanism occurred between the IBF compound and the membranes during the dark filtration mode, which led to the minimal fouling phenomenon [45].

When the light was turned on, the flux trend of the pristine PVDF remained stable throughout the test whether light was turned on or not, whereas for the flux of PVDF-ZAA MMMs, there was a positive response within 180 min of filtration. The PVDF-ZAA₁ membrane was found to have the highest IBF filtration rate, with the flux increasing up to 60% compared with the dark filtration mode. In fact, all of the MMMs experienced a significant filtration improvement from the dark filtration, with an increase of 15.48%, 17.86%, and 129.93% in the light filtration mode for PVDF-ZAA_{0.5}, PVDF-ZAA₂, and PVDF-ZAA₃, respectively. A fascinating result found that in the first 60 min of IBF filtration, all fluxes for the MMMs were slightly higher than their initial flux. As presented in the relative flux shown in Figure 5d, all MMMs portrayed a fascinating photo-filtration behavior, with an IBF permeation higher than a ratio value of 1, signifying that none of the MMMs experienced flux loss. Such improvement was ascribed to the photodegradation of IBF during penetration through the membrane pores, restraining the membrane fouling to some extent. In particular, PVDF-ZAA₃ demonstrated superior performance (with a flux ratio reaching about 1.3), which is consistent with its smallest band gap value (1.8 eV) (see Figure S2). It was found that the drawback of the unevenness and rougher membrane surface turned out to be an advantage for the photo-filtration reaction. However, PVDF-ZAA₃ remained the lowest IBF permeation among the membranes. Overall, the incorporation of ZnO/Ag₂CO₃/Ag₂O enhances the membrane's antifouling capability, where the continuous irradiation of visible light would inhibit the solute layer over the membrane surface. This enhancement in antifouling performance has been reported elsewhere, where membranes incorporated with photocatalysts exhibited such a phenomenon [46,47]. As a result, the incorporation of the ZnO/Ag₂CO₃/Ag₂O visible driven photocatalyst for photocatalytic membrane applications could enhance the membrane water flux and mitigate the membrane fouling phenomenon.

2.6. Ibuprofen Removal Efficiency

Regarding the molecular weight of IBF of 206 g/mol, it is much lower than the nominal MWCOs of the UF membranes (3000 Da) tested in this study [48,49]. As a consequence, it is unlikely that an "exclusion mechanism" would be effective in removing IBF from UF membranes. However, the removal of IBF by the prepared membranes in Figure 6 showed

remarkable performance, with PVDF-ZAA_{0.5} exhibiting the best removal performance (26.93%), followed by PVDF-ZAA₂ (25.27%), PVDF-ZAA₃ (24.52%), PVDF-ZAA₁ (22.47%), and pristine PVDF (20.04%). This enhancement in IBF removal for the membranes incorporated with ZnO/Ag₂CO₃/Ag₂O can be ascribed to the “electrostatic repulsion mechanism”, since, as previously mentioned, the pK_a of ibuprofen is 4.50, which is mostly deprotonated in neutral pH, resulting in a negative charge state. While all of the tested membranes had negative zeta potential (in pH neutral), both molecules and membranes had negative charge values at the operating pH. Thus, in dark conditions, charge repulsion (the Donnan effect) became the reason for the IBF removal [45]. Park et al. [50] also reported that charge repulsion could become a primary mechanism for IBF removal in UF systems.

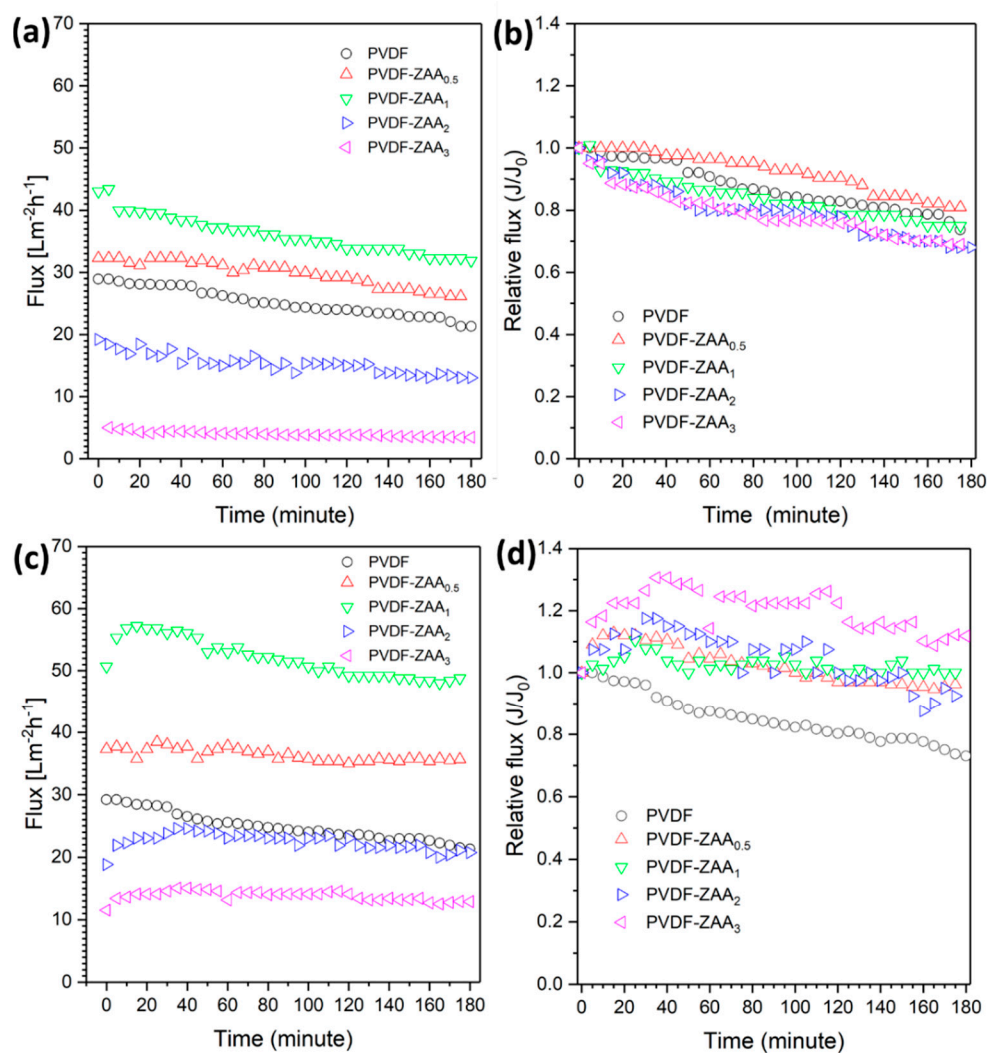


Figure 5. IBF permeation in (a,b) the darkness and (c,d) under visible light irradiation for the prepared membranes.

However, some researchers asserted that the removal of IBF may occur as a result of hydrophobic adsorption [45,51]. According to Singh et al. [52], the photodegradation of IBF was shown to be most effective in acidic conditions. Under basic conditions, both photocatalytic membranes and IBFs produced deprotonated species, but photocatalytic activity still occurred even at lower degradation levels [53]. As mentioned by Oyetade et al. [53], hydrogen bonds accounted for only a small fraction of the overall binding, whereas hydrophobic interactions accounted for most of the adsorption across a pH range. Since the experiment was conducted at neutral pH, the IBF molecules could have hydrophobic interactions with the PVDF-ZAA membrane’s surfaces. At the same time, the electrostatic potential lessens

the effect of hydrophobic interactions, which reduces—but does not eliminate—binding. Accordingly, Kim et al. [45] reported that the removal of IBF with UF membranes (MWCO 3000 Da) at pH neutral was, surprisingly, found to remove over 50% of IBF, retained by the electrostatic repulsion mechanism and hydrophobic adsorption effect. In terms of IBF removal performance, PVDF-ZAA₁ has been found to be the lowest among MMMs due to the highest IBF flux rate, as seen from Figure 6a. It is a well-established fact that higher flux leads to lower solute removal, which correlates to the increment in higher membrane pore count and porosity [54]. Overall, no significant changes in IBF removal were detected throughout the dark filtration period.

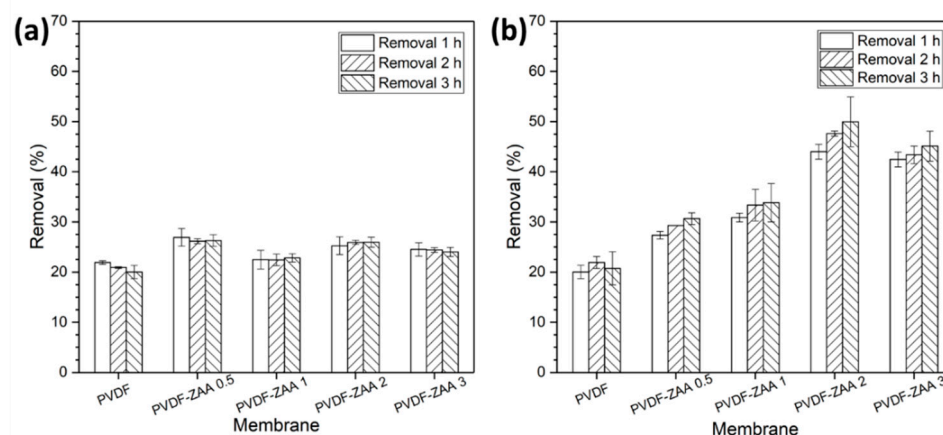


Figure 6. Removal of IBF in the dark (a) and under visible light irradiation (b) for 3 h by the prepared membrane.

When the membranes were tested with visible light, all of the PVDF-ZAA MMMs in Figure 6b revealed a progressive increase in IBF removal, with a higher removal rate within 3 h of IBF filtration. Among these membranes, PVDF-ZAA₂ remained the best at removal, achieving 43.98% removal in the first 60 min of filtration, followed by PVDF-ZAA₃ (42.47%), PVDF-ZAA₁ (30.87%), and PVDF-ZAA_{0.5} (27.36%). The increased IBF removal can be accredited to the photocatalytic response to IBF photodegradation. It is in accordance with the optical properties of MMMs, which are highly reactive to the visible light response, as referred to in Figure S2. Consequently, all of these IBF removals suggest that removal is affected by the simultaneous action of charge effect (i.e., electrostatic repulsion), hydrophobic adsorption, and photocatalytic activity. This is due to the lower rate of IBF removal presented in Figure 6b, even with the lower band gap. This correlates with a higher IBF flux rate that resulted in a significant decrease in its photocatalytic efficiency due to the short contact time of IBF during photocatalytic activity. Studies by Moustakas et al. [55] indicated that the higher effluent flow rate through the pores of the membrane lead to a remarkable decrease in its photocatalytic efficacy due to the shorter contact time between the pollutant and the photocatalytic surface.

The improvement of IBF removal using the photocatalytic filtration of PVDF-ZAA MMMs within 3 h between the dark conditions and the visible light illumination is presented in Figure 7. According to the figure, pristine PVDF has a negative improvement in IBF degradation as it is irradiated under illumination. On the other hand, PVDF-ZAA₃ and PVDF-ZAA₂ both showed a significant increase in IBF removal in visible light compared to dark conditions, with 87.7% and 92.4% improvement after 3 h of light exposure, respectively. It has been observed that PVDF-ZAA₃ has a slower IBF flux rate, which prolongs the contact time of the IBF molecule with the membrane surface. The low IBF flux penetrating through the tight pore structure of the membrane is beneficial for photocatalytic activity, since it allows enough time for IBF to degrade. More importantly, the higher IBF removal of PVDF-ZAA₂ and PVDF-ZAA₃ was due to their lower band gap energy, which is 2.0 and 1.8 eV, respectively (see Figure S2b). Their ability to absorb a

higher fraction of photons from visible light irradiation clearly affected the changes in IBF removal. It should also be noted that the higher IBF removal rates were also associated with higher membrane roughness that favors hydrophobic adsorption and a photocatalytic mechanism. Even though PVDF-ZAA₃ has the lowest band gap value, it lost some of its photocatalytic activity due to the excessive agglomeration of photocatalysts, resulting in a lower exposure of ZnO/Ag₂CO₃/Ag₂O indirectly. Therefore, the PVDF-ZAA₃ mixed matrix membrane was expected to exhibit a slight decrease in its photocatalytic activity. Overall, an addition of 1.96 wt% of ZnO/Ag₂CO₃/Ag₂O to the PVDF membrane exhibited the highest photocatalytic filtration activity when irradiated with visible light.

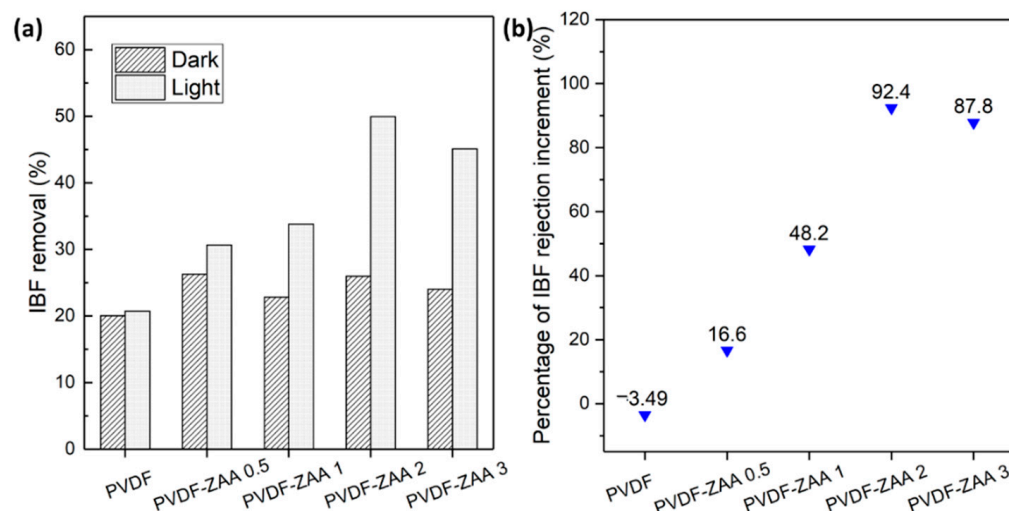


Figure 7. (a) IBF removal in the dark and light irradiation after 3 h; (b) percentage of removal increment of IBF, before and after light irradiation after 3 h.

The UV-Vis spectra of the feed and permeate solutions of IBF filtration in visible light irradiation in Figure 8a show the existence of IBF molecules (222 nm) in the feed and the IBF penetrant in permeate. The IBF penetrant was predicted as lower than the IBF feed due to the charge effect, hydrophobic adsorption, and photocatalytic activity. Meanwhile, the IBF feed experienced photodegradation with increasing time. The degradation of IBF can be attributed to the photodegradation via hydrophobic adsorption over the membrane surfaces, leading to a decrease in absorbance at 222 nm.

In addition, the presence of IBF by-product degradation (intermediate compound) in the feed is also indicated by the residual peak between 240–300 nm (see Figure 8a). The by-product of IBF degradation at 263 nm in the feed showed a higher absorption peak in the first and second hour of photo-filtration. The higher absorption in 263 nm signified that a higher intermediate compound was produced during the degradation of the IBF molecules. This implies that an active photocatalytic degradation of IBF occurred in the feed solution over the membrane surface, increasing the IBF removal in permeate. On the other hand, the permeate quality shows the presence of an intermediate compound in the IBF permeate that is lower than that in the IBF feed. This situation could be attributed to the additional photocatalytic activity in the membrane pores lowering the intermediate peak value.

The photographs of the membrane collected after 3 h of IBF filtration in the dark and under visible light irradiation are shown in Figure 8b. As can be seen, the membrane irradiated with light was found to be darker, signifying that the photocatalytic activity actively occurred on the membrane surface. This is in accordance with Rosman et al. [26], who found that ZnO/Ag₂CO₃/Ag₂O experienced a repeated reduction process during light illumination, forming metal clusters and Ag⁰ (Ag⁺ + e⁻ → Ag⁰) [56]. The dark colour of the exposed membrane signifies the presence of Ag⁰ in response to ZnO/Ag₂CO₃/Ag₂O photocatalytic activity.

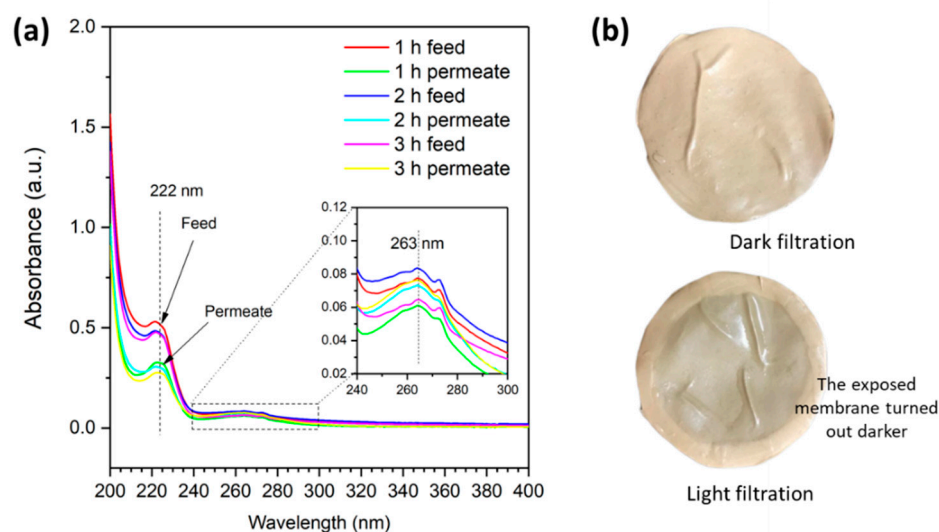


Figure 8. (a) UV–Vis spectra of the feed and permeate of IBF photo-filtration run under visible light irradiation for the PVDF-ZAA₂ membrane; (b) photograph of the membrane collected after three hours of IBF filtration.

2.7. Membrane Recyclability Studies

The membrane recyclability of photo-filtration has been evaluated to study the behavior of membrane reusability and its antifouling capabilities. A representative PVDF-ZAA₂ membrane was used for three cycles of IBF filtration, and the results are shown in Figure 9a. Based on the figure, it can be seen that the IBF permeability of PVDF-ZAA₂ increased with permeation time, and slightly decreased towards the end of each cycle. Upon each cleaning cycle with DI water under light irradiation for 30 min, it is surprising that the photo-filtration of PVDF-ZAA₂ intermittently experienced rising flux in each cycle. This increment could be attributed to the constant contact between the photocatalyst in the membrane and the IBF solution, resulting in photocatalytic degradation. Towards the end of the cycle, the second and third cycle showed the IBF flux slightly reduced below its initial flux. This could be due to the undegraded IBF passing through the membrane's pores, leading to pore narrowing/clogging. However, the flux was recovered in every cycle, which resulted in high flux recovery increments in the IBF permeation (as portrayed in Figure 9b). This signifies the unattachment of IBF owing to its negative hydrophobic nature, which is easy to clean via light irradiation and the washing method. Apart from that, the photocatalyst in the membrane was able to degrade relatively high levels of IBF over multiple cycles of five hours each. The explanation behind this phenomenon is the continuous photoinduced hydrophilicity of PVDF-ZAA₂ upon light irradiation, which allowed for higher water affinity and led to IBF removal selectivity.

Additionally, the role of ZnO/Ag₂CO₃/Ag₂O in MMMs to generate surface redox reaction allowed the photodegradation of IBF molecules attached to the membrane surface. This resulted good IBF removal recovery, as portrayed in Figure 9b. Removal was 42.22% after the third cycle of photo-filtration, which brings the removal recovery up to 99.01%. The slight increase in the IBF removal with the increasing photo-filtration cycle could be explained by the photoinduced hydrophilicity on the membrane pores and surface that increased the density of the active photocatalytic sites. Moreover, the ability of the ZnO/Ag₂CO₃/Ag₂O photocatalyst to be recycled up to three times with over 90% of IBF degradation under visible light irradiation, as shown in a previous study [26], signifies that the photocatalyst could remain stable even when incorporated into the membrane. Overall, the PVDF-ZAA₂ photocatalytic membrane has the potential for reusability via light-assisted self-cleaning.

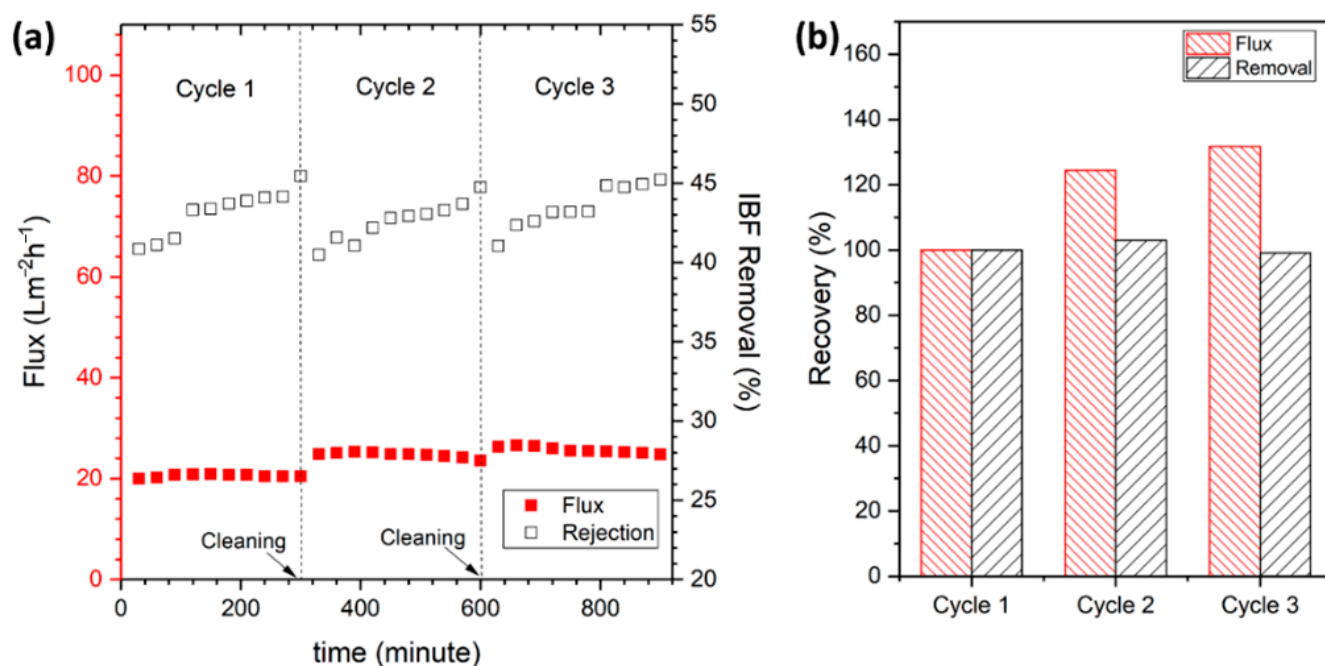


Figure 9. Reusability potential of the PVDF-ZAA₂ MMM: (a) specific IBF removal and flux performance with inter-cycle cleaning in the presence of light irradiation; (b) percentage of flux and removal recovery within 300 min.

2.8. Mechanism for Enhanced Antifouling Performance

Based on all of the results and the discussion of the photo-filtration experiment, a proposed mechanism was discussed for the development of the photo-filtration properties of PVDF-ZAA MMMs. It was noted that PVDF-ZAA₂ exhibited a band gap value of 2.0 eV; hence, it offers a much higher photon absorption with a larger interaction with the pollutant due to its rougher membrane surface, suggesting an entrapment of IBF with better photodegradation activity. However, due to the electronegatively charged PVDF and IBF, the degradation of IBF was only possible due to the interaction with the ZnO/Ag₂CO₃/Ag₂O photocatalyst. The reason is that under neutral conditions, the zeta potential of ZnO/Ag₂CO₃/Ag₂O is -6.040 ± 0.833 mV, which is less deprotonated than the membrane surface (-34.6 mV). Hence, the photocatalyst is reported to have lower electrostatic repulsion and to preferentially undergo photocatalytic activity. However, based on the flux observation of PVDF-ZAA MMMs, the flux became higher as the light irradiation was continuously operated. Meanwhile, the IBF flux of the PVDF pristine membrane (Figure 5) remained unchanged throughout the test whether the light was stimulated or not. Thus, this situation required an extended explanation regarding this phenomenon.

Put simply, the photocatalyst experienced surface hydroxylation produced from the photocatalyst to trigger the degradation of the pollutant molecules [57]. Pan et al. [58] studied this phenomenon as a way to promote the favorably adsorbed molecules that react more efficiently with the light. Their study showed that •OH radicals underwent hydroxylation–rehydroxylation conditions. The rehydroxylation allows short-lived •OH generation on the photocatalyst surfaces, rapidly converting to catalytically inactive surface hydroxyls [55]. Several groups have investigated the effect of rehydroxylation on the photocatalyst surface and have confirmed that it contributes to a higher photodegradation rate [59]. In this study, based on Figure S3, Ag₂CO₃ mainly underwent a hydroxylation–rehydroxylation reaction due to being the main source of hydroxyl radical generation. The rehydroxylation reaction is the process in which the •OH radicals turn into catalytically inactive surface hydroxyls, leading to a saturated OH layer [60,61] that is charged in the selective adsorption of IBF molecules. Hence, the saturated OH layer that is formed from the rehydroxylation reaction is a response of the IBF flux increment as the light is irradiated.

This is because the possibility of light inducing a flux increase or interacting with the PVDF membrane to cause pore deformation is unconvincing. However, with the presence of ZnO/Ag₂CO₃/Ag₂O embedded in the PVDF matrix, the photoinduced hydrophilicity effect on the MMMs due to rehydroxylation subsequently increases the IBF flux. This is supported by a recent study by Tran, Mendret, Méricq, Faur, and Brosillon [13], which revealed that the increased hydrophilicity was responsible for the rise in the pure water flux during photo-filtration, as layers of water were more easily attracted and quickly transported through the membranes. The response of flux increments due to photoinduced hydrophilicity has also been discussed by Wang et al. [62]. In this way, the membrane is possibly hydrophilized as the light is irradiated; hence, more water is attracted to pass through the membrane, while the IBF is retained over the membrane surfaces to be photodegraded by the ZnO/Ag₂CO₃/Ag₂O nanoparticles. Meanwhile, as hydroxylation takes place, •OH radicals continually undergo IBF mineralization.

Thus, a cooperative effect between the Ag₂CO₃, Ag₂O, and ZnO heterojunctions absorbs the photon energy to generate the excited electron–hole, following the Z-scheme/Type I mechanism in Figure S3, which certainly accounts for the IBF degradation. In fact, the generation of •OH, H⁺, and •O₂[−] radicals also introduces a new membrane photocatalytic mechanism that generates surface rehydroxylation for photoinduced hydrophilicity to achieve better membrane filtration, and surface hydroxylation for enhanced IBF removal. In this sense, the membrane's surface experienced hydroxylation-rehydroxylation activating hydrophilicity and photocatalytic filtration, thereby enhancing the removal of IBF. Moreover, the incorporation of ZnO/Ag₂CO₃/Ag₂O alters the membrane's morphological and surface properties to create a rougher membrane surface, allowing for a good interaction of the membrane and the IBF molecules throughout the photodegradation processes. Therefore, the incorporation of ZnO/Ag₂CO₃/Ag₂O in the PVDF membrane was found to be beneficial for water filtration enhancement without removal and membrane fouling phenomena. The schematic illustration of the photo-filtration of PVDF-ZAA MMMs is shown in Figure 10.

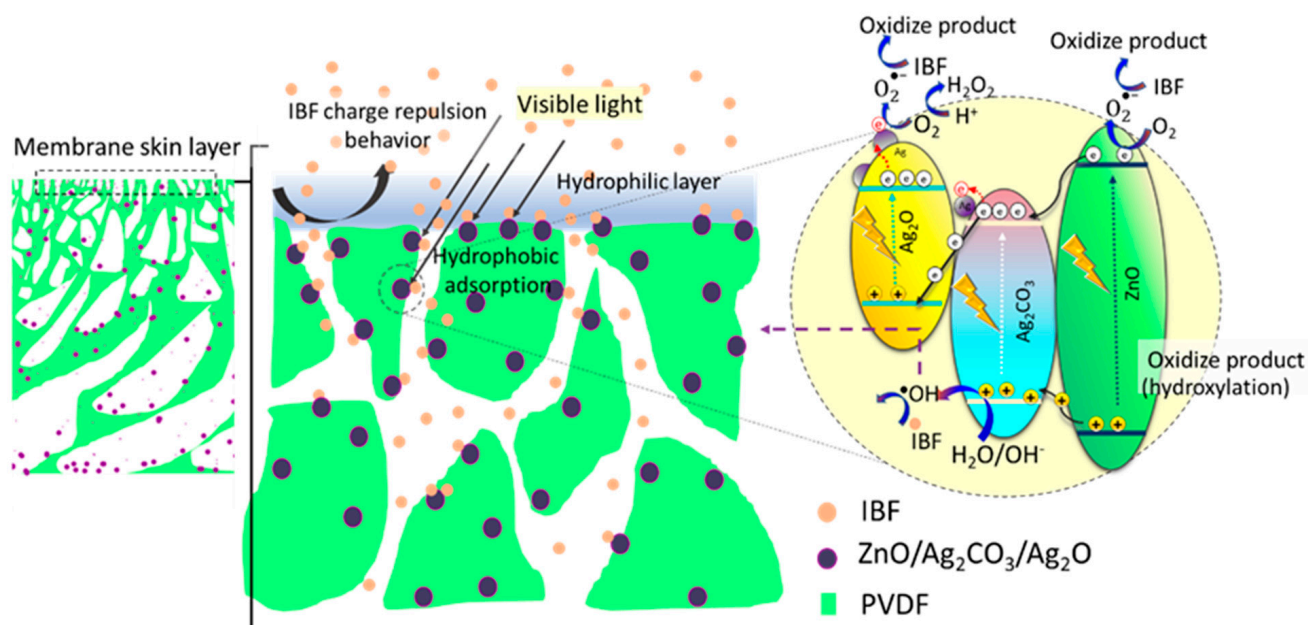


Figure 10. Schematic illustration of IBF photodegradation with PVDF-ZAA₂ MMMs. Enlarged image is the photocatalytic mechanism of ZnO/Ag₂CO₃/Ag₂O.

3. Methodology and Characteristics

3.1. Materials

All chemicals chosen in this study were of analytical grade and used as purchased without any further purification. The analytical grade chemicals from different suppliers

included zinc acetate dihydrate ($C_4H_6O_4Zn \cdot 2H_2O$, HmbG, Hamburg, Germany), silver nitrate ($AgNO_3$, Sigma Aldrich, Steinheim am Albuch, Baden-Württemberg, Germany), and sodium bicarbonate ($NaHCO_3$, Bendosen Laboratory Chemicals, Bendosen, Norway). In the membrane development, poly (vinylidene fluoride) (PVDF) 760, polyvinylpyrrolidone (PVP K-30, 40 kDa), and lithium chloride (LiCl) were used as pore formers. *N*-methyl-2-pyrrolidone (NMP) from Sigma-Aldrich, Steinheim am Albuch, Baden-Württemberg, German, was used as a solvent. On the other hand, the membrane fabrication utilized poly (vinylidene fluoride) (PVDF, Solvay Advanced Polymers, Brussels, Belgium) as a polymer base and *N*-Methyl-2-pyrrolidone (NMP (99.5%), Merck, Darmstadt, Germany) as a solvent. The synthetic ibuprofen (Merk, St. Louis, Missouri) was used to prepare the pharmaceutical pollutant. All solutions were prepared using deionized water.

3.2. Preparation of the Photocatalyst

A $ZnO/Ag_2CO_3/Ag_2O$ photocatalyst was synthesized based on our previous study [26]. As a first step, 10.0 g of $Zn(Ac)_2 \cdot 2H_2O$ were ground for 30 min with a mortar and directly calcined at 450 °C at a rate of 10 °C min^{-1} under atmospheric conditions for 2 h. Then, 1.5 g of ZnO was suspended in 40 mL of ultrapure water along with 0.336 g of $NaHCO_3$. For the synthesis of ZnO/Ag_2CO_3 , the dropwise addition of 20 mL of aqueous $AgNO_3$ solution (1.358 g) was performed after the solution was stirred at room temperature. In an 18-h stirring period, a greyish yellow suspension of ZnO/Ag_2CO_3 was produced, filtered, washed three times with deionized (DI) water, and dried at 60 °C overnight. The ZnO/Ag_2CO_3 was calcined under atmospheric conditions for 8 min at 195 °C before being removed for the instantaneous formation of $ZnO/Ag_2CO_3/Ag_2O$ heterojunctions.

3.3. Preparation of Mixed Matrix Membrane (MMMs)

The MMM was fabricated by wet phase inversion in a single casting step based on our previous research [63]. Initially, various weight percentages of $ZnO/Ag_2CO_3/Ag_2O$ were added to the membrane dope solution. As a reference membrane, 18 wt% of PVDF membranes were prepared without any fillers. PVP and LiCL powder was added to a constant quantity of 0.5 wt% and 2 wt%, respectively, for the entire period of the experiment. A mixture of NMP/PVP/LiCL was stirred at 65 °C to completely dissolve the PVDF pellet. Consequent to this preparation, a pristine PVDF membrane was obtained and labeled PVDF. To investigate the impact of $ZnO/Ag_2CO_3/Ag_2O$ loading, 0.5 wt% of $ZnO/Ag_2CO_3/Ag_2O$ was first dissolved in an NMP solution and sonicated for 10 min to achieve homogeneous particle distribution before it was mixed with PVP, LiCL, and 18 wt% of dried PVDF pellets. The dope mixture was left stirring overnight to achieve a homogenous dope solution. Next, the solution was degassed for an hour to ensure that all bubbles were removed completely. The same procedure was repeated for preparing the dope solutions for loading 1–2.91 wt% $ZnO/Ag_2CO_3/Ag_2O$. The dope was labeled with PVDF-ZAA_{0.5}, PVDF-ZAA₁, PVDF-ZAA₂, and PVDF-ZAA₃ for 0.5, 0.99, 1.96, and 2.91 wt% of $ZnO/Ag_2CO_3/Ag_2O$ photocatalyst loading, respectively. In the preparation of the membrane, dope was poured onto a glass plate, and the solution was spread onto the glass plate using a glass rod. As soon as the solvent had evaporated for 30 s, the plate was placed in a coagulation bath and the membrane formed slowly. The membrane detached itself from the glass plate after several minutes. After solidification, the membranes were left overnight to remove all residual solvent, thereby allowing them to solidify entirely. Then, the membrane was made available for use after it had been air dried at room temperature for two days.

3.4. Photocatalyst Characteristics

The prepared photocatalyst was characterized to study its properties using analytical instruments, such as transmission electron microscopy (HT 7700 Hitachi, TEM, Tokyo, Japan) for phase analysis, X-ray Diffraction (Bruker D8 Advance diffractometer, XRD, Karlsruhe, Germany) for crystallinity analysis, and ultraviolet-visible spectroscopy

(Lambda 1050 UV/VIS/NIR Spectrometer, PerkinElmer, Waltham, MA, USA) for optical property changes.

3.5. Membrane Characteristics

The effect of ZnO/Ag₂CO₃/Ag₂O loading on the fabrication of the PVDF mixed matrix membrane was further analyzed under various characterization analyses. The surface and cross-section morphology of the membrane was determined via scanning electron microscopy analysis. The membrane samples were examined using Hitachi TM3000 Tabletop scanning electron microscope (Hitachi High-Technologies Corporation, SEM, Tokyo, Japan). The membrane was selectively chosen and cut into dimensions of 0.5 cm × 0.5 cm, wherein it was attached to an aluminum specimen stub using double-sided carbon tape. Meanwhile, the cross-section of the membrane was attained using the freeze–fracture technique. The membrane samples were first immersed in liquid nitrogen until the membrane began to solidify, and instantaneously broken using tweezers. Then, the fractured membrane was deemed ready to be attached to the aluminum specimen stud with double-sided carbon tape. Before undergoing SEM analysis, the tested membrane on the aluminum stud was sputter coated with platinum using sputter coating. Energy dispersive X-ray analysis (EDX), which is built into the SEM equipment, was used to analyze the elemental composition of the membrane sample.

Meanwhile, the surface topography and roughness of the top membrane were investigated using atomic force microscopy (XE-100 Park Systems, AFM, Suwon, South Korea). Prior to AFM analysis, a small piece of each membrane was cut and pasted on the top of a 2-cm² round sample holder. In AFM, the laser light is reflected from the cantilever and detected by a photodiode. The AFM tip functioned when it contacted or nearly contacted the surface of interest to generate the surface profiles of the membrane samples. Three measurements of roughness parameters (R_a , R_q , and R_z) were taken using Image Analysis P9 (NT-MDT, Zelenograd, Russia) software. The optical absorption behavior of the MMMs was investigated using a UV-Vis-NIR spectrophotometer (UV-3101PC, Shimadzu, Kyoto, Japan). This characterization was important to determine the light absorption capability of the prepared membrane under different wavelength radiations. The sample was directly mounted on a sample holder and scanned at a wavelength between 200 and 800 nm. Meanwhile, the band gap energy of the prepared membrane was estimated using the Kubelka–Munk function, where it was estimated by plotting $(\alpha h\nu)^{1/2}$ versus the energy of absorbed light.

The membrane hydrophilicity was investigated by measuring the contact angle (CA). A dynamic CA measurement by the sessile drop method was carried out via the G1 model, KRÜSS GmbH, Hamburg, Germany, and the liquid used for the CA test was RO water. A sample was prepared by cutting the membrane into pieces with dimensions of 0.5 × 5 cm at random positions. These samples were placed on the stage and fixed to the sample holder. Then, a syringe filled with RO water was installed. The syringe needle was adjusted 18 mm above the membrane surface. The water was injected onto the membrane surface and images of the membrane's water absorption behavior were recorded within 120 s. Then, the membrane was further examined for its porosity characteristics. The porosity was calculated via the volume of the pores per the total volume of the porous membrane, as per Equation (1) [25].

$$\text{porosity, } \varepsilon (\%) = \frac{w_{wet} - w_{dry}}{v_m \times \rho_w} \times 100 \quad (1)$$

where ε is the membrane's overall porosity (%), w_{wet} is the weight of wet membrane (g), w_{dry} is the weight of the dry membrane (g), v_m is the volume of the membrane (cm³), and ρ_w is the density of water (g/cm³). Meanwhile, the membrane water uptake was evaluated using the different values of the wet and dry membrane.

3.6. Membrane Performance

The prepared MMMs were evaluated in IBF permeation and removal in dark and visible light irradiation within 180 min under a membrane photo-filtration experimental system, as seen in Figure 11. To evaluate the photo-filtration activity of the prepared PVDF-ZnO/Ag₂CO₃/Ag₂O MMMs at different photocatalyst loadings (0–2.91 wt%), 10 ppm of 300 mL IBF was used as a model of water pollutant. The active filtration area of the membrane was 12.56 cm². A white light-emitting diode (LED) lamp ($\lambda > 400$ nm, 100 W) was used as the visible light source in the membrane photocatalytic filtration system.

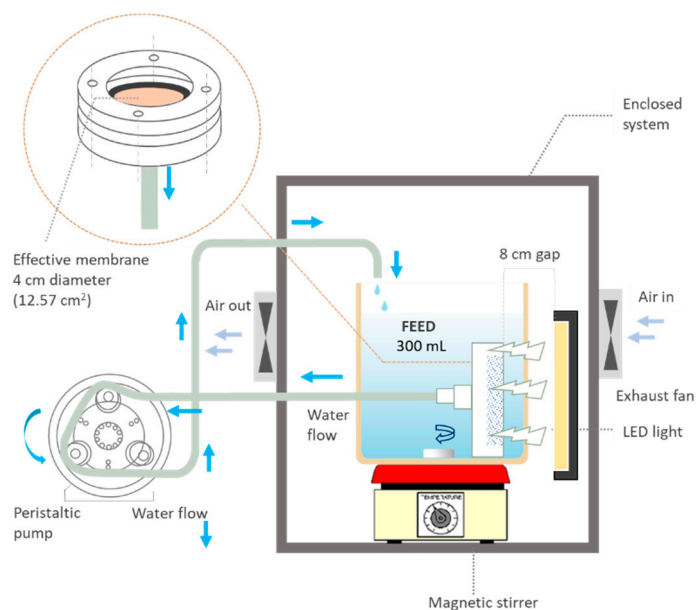


Figure 11. Membrane photo-filtration experimental setup.

Prior to each experiment, the membrane was left in IBF solution in the dark for 60 min to achieve adsorption–desorption equilibrium without circulating the permeate solution back into the reactor. Then, the process continued with another 30 min of circulation, where 3 mL of permeate was collected as the initial concentration of IBF (C_0). Prior to the photo-filtration process, the membrane was left irradiated under visible light irradiation for 30 min before the pump was turned on. Then, the IBF flux was measured every five minutes and the permeated IBF was placed back into the IBF feed container. This was to ensure the homogenous condition of the IBF concentration in the tank. All experiments were performed at room temperature (27 ± 1 °C). The same procedure was repeated to collect treated permeates for IBF removal evaluation at 60-min intervals within 180 min of the experimental period. The degradation of IBF was monitored using a PerkinElmer UV-Vis spectroscopy to measure the change of IBF concentration throughout the experiment at 222 nm. The performance of the prepared MMMs was evaluated by the concentration of IBF for each collected sample. The photocatalytic activity was expressed in percentage of ibuprofen degradation, according to the Equation (2):

$$\text{Removal of IBF in photo-filtration (\%)} = \left[1 - \frac{C_p}{C_f} \right] \times 100 \quad (2)$$

where C_p and C_f are the concentrations of IBF in permeate (ppm) and initial feed (ppm), respectively. For the membrane filtration process, each IBF permeate sample was taken every 60 min and measured using Equation (3).

$$J_{IBF} = \frac{V}{A \times \Delta t} \quad (3)$$

The membrane was further tested for membrane recyclability, which lasted for 300 min and collected every 30 min, with a similar experimental setup that followed the membrane photo-filtration performance. However, the membrane was filtered with RO water for every cycle at 30 min with light irradiation. A total of three filtration cycles were conducted to determine membrane reusability, based on Equations (4) and (5).

$$F_R = \frac{F_w}{F_i} \times 100\% \quad (4)$$

where F_R is the flux recovery percentage, F_i is the initial cycle of IBF flux, and F_w is the IBF flux for the next cycle. For recovery, the removal properties were analyzed based on the following equation:

$$R_R = \frac{R_w}{R_i} \times 100\% \quad (5)$$

where R_R is the IBF removal recovery percentage, R_i is the initial cycle removal, and R_w is the removal recovery for the next cycle after the membrane is subjected to RO water purification.

4. Conclusions

ZnO/Ag₂CO₃/Ag₂O was successfully incorporated into the PVDF membrane for advanced membrane antifouling and photocatalytic water purification. SEM images showed that the incorporation of ZnO/Ag₂CO₃/Ag₂O at a 0.99 wt% loading in the PVDF polymer matrix exhibited obvious agglomeration and rougher membrane surfaces. However, water contact angle measurements showed that the MMMs had a lower water contact angle, which implies improved membrane hydrophilicity. These situations resulted in a significant effect on the membrane properties, such as the IBF flux and antifouling performance. By testing its photocatalytic filtration performance, the higher photocatalyst loading had a positive effect despite its lower flux rate and rougher membrane surfaces. The resulting PVDF-ZnO/Ag₂CO₃/Ag₂O membrane with a rougher membrane surface area, lower flux rate, and excellent light harvesting capability demonstrated good photocatalytic filtration activity in removing IBF under visible light irradiations. In fact, the fluxes of all the MMMs demonstrated higher IBF fluxes than their initial fluxes at certain durations, signaling that the membrane actively responded to light irradiation. The positive flux increase can be ascribed to the photoinduced hydrophilicity generated by the ZnO/Ag₂CO₃/Ag₂O photocatalyst, resulting in easier water layer formation, and swifter transport through the membranes. Furthermore, the MMMs with a higher ZnO/Ag₂CO₃/Ag₂O photocatalyst loading achieved higher IBF removal. Among the membranes, the highest IBF removal was achieved by PVDF-ZAA₂ (1.96 wt% loading), with 49.96% of IBF removal within 180 min upon visible light activation. The recyclability of PVDF-ZnO/Ag₂CO₃/Ag₂O also showed a great improvement, with 99.01% of IBF removal recovery after three cycles. These results highlight the potential of such hybrid membranes in mitigating membrane fouling while providing a platform for the photocatalyst to continuously degrade pollutants present in such wastewaters. Hence, the hybridization of photocatalytic membranes provides valuable insight for expansion and retrofitting into the current water effluent treatment process for water reclamation purposes.

Supplementary Materials: The following are available online at <https://www.mdpi.com/article/10.3390/catal12020209/s1>, Figure S1: (a) TEM image; (b) SAED pattern; (c) XRD of ZnO/Ag₂CO₃/Ag₂O photocatalyst; and (d) the band gaps value of prepared photocatalyst, Figure S2: (a) UV-vis absorption spectra for PVDF-ZAA membrane with different loading of ZnO/Ag₂CO₃/Ag₂O. (b) $(\alpha h\nu)^{1/2}$ versus vs the energy of absorbed light affords the band gaps of the different samples; Figure S3: Schematic illustration for the photocatalytic reaction process of the ZnO/Ag₂CO₃/Ag₂O heterostructures under LED light irradiation (a) Type II/Type I and (b) Z scheme/Type I mechanism

Author Contributions: Conceptualization, methodology, formal analysis, investigation, and writing—original draft preparation, N.R.; resources, writing—review and editing; project administration, W.N.W.S.; formal analysis, investigation, J.J.; supervision, Z.H.; writing—review and editing F.A.; funding acquisition, A.F.I. All authors have read and agreed to the published version of the manuscript.

Funding: This research was funded by the Ministry of Education and Universiti Teknologi Malaysia under the Higher Institution Centre of Excellence Scheme (Project Number: R. J090301.7851.4J423) and UTM High Impact Re-search (Project Number: Q. J130000.2451.08G36).

Data Availability Statement: The physicochemical of photocatalyst can be found in [26].

Acknowledgments: The authors gratefully acknowledge the financial support from the Ministry of Education and Universiti Teknologi Malaysia under the Higher Institution Centre of Excellence Scheme and UTM High Impact Research. The authors would also like to acknowledge the technical and management support from the Research Management Centre (RMC), Universiti Teknologi Malaysia.

Conflicts of Interest: The authors declare no conflict of interest.

References

1. Petrie, B.; Barden, R.; Kasprzyk-Hordern, B. A review on emerging contaminants in wastewaters and the environment: Current knowledge, understudied areas and recommendations for future monitoring. *Water Res.* **2015**, *72*, 3–27. [[CrossRef](#)]
2. Richardson, B.J.; Lam, P.K.; Martin, M. Emerging chemicals of concern: Pharmaceuticals and personal care products (PPCPs) in Asia, with particular reference to Southern China. *Mar. Pollut. Bull.* **2005**, *50*, 913–920. [[CrossRef](#)] [[PubMed](#)]
3. Dhar, D.; Roy, S.; Nigam, V.K. Advances in protein/enzyme-based biosensors for the detection of pharmaceutical contaminants in the environment. In *Tools, Techniques and Protocols for Monitoring Environmental Contaminants*; Elsevier: Amsterdam, The Netherlands, 2019; pp. 207–229.
4. Celiz, M.D.; Tso, J.; Aga, D.S. Pharmaceutical metabolites in the environment: Analytical challenges and ecological risks. *Environ. Toxicol. Chem.* **2009**, *28*, 2473–2484. [[CrossRef](#)] [[PubMed](#)]
5. Daughton, C.G.; Ternes, T.A. Pharmaceuticals and personal care products in the environment: Agents of subtle change? *Environ. Health Perspect.* **1999**, *107*, 907–938. [[CrossRef](#)] [[PubMed](#)]
6. Emmanuel, E.; Perrodin, Y.; Keck, G.; Blanchard, J.-M.; Vermande, P. Ecotoxicological risk assessment of hospital wastewater: A proposed framework for raw effluents discharging into urban sewer network. *J. Hazard. Mater.* **2005**, *117*, 1–11. [[CrossRef](#)]
7. Tauxe-Wuersch, A.; De Alencastro, L.F.; Grandjean, D.; Tarradellas, J. Occurrence of several acidic drugs in sewage treatment plants in Switzerland and risk assessment. *Water Res.* **2005**, *39*, 1761–1772. [[CrossRef](#)]
8. Brozinski, J.-M.; Lahti, M.; Meierjohann, A.; Oikari, A.; Kronberg, L. The anti-inflammatory drugs diclofenac, naproxen and ibuprofen are found in the bile of wild fish caught downstream of a wastewater treatment plant. *Environ. Sci. Technol.* **2013**, *47*, 342–348. [[CrossRef](#)]
9. Bragança, I.; Plácido, A.; Paíga, P.; Domingues, V.F.; Delerue-Matos, C. QuEChERS: A new sample preparation approach for the determination of ibuprofen and its metabolites in soils. *Sci. Total Environ.* **2012**, *433*, 281–289. [[CrossRef](#)]
10. Weigel, S.; Berger, U.; Jensen, E.; Kallenborn, R.; Thoresen, H.; Hühnerfuss, H. Determination of selected pharmaceuticals and caffeine in sewage and seawater from Tromsø/Norway with emphasis on ibuprofen and its metabolites. *Chemosphere* **2004**, *56*, 583–592. [[CrossRef](#)] [[PubMed](#)]
11. Huerta-Fontela, M.; Galceran, M.T.; Ventura, F. Occurrence and removal of pharmaceuticals and hormones through drinking water treatment. *Water Res.* **2011**, *45*, 1432–1442. [[CrossRef](#)]
12. Hassaan, M.A.; El Nemr, A. Advanced oxidation processes for textile wastewater treatment. *Int. J. Photochem. Photobiol.* **2017**, *2*, 85–93.
13. Tran, D.-T.; Mendret, J.; Méricq, J.-P.; Faur, C.; Brosillon, S. Study of permeate flux behavior during photo-filtration using photocatalytic composite membranes. *Chem. Eng.* **2020**, *148*, 107781. [[CrossRef](#)]
14. Lv, Y.; Zhang, C.; He, A.; Yang, S.J.; Wu, G.P.; Darling, S.B.; Xu, Z.K. Photocatalytic nanofiltration membranes with self-cleaning property for wastewater treatment. *Adv. Funct. Mater.* **2017**, *27*, 1700251. [[CrossRef](#)]
15. Zheng, X.; Shen, Z.-P.; Shi, L.; Cheng, R.; Yuan, D.-H. Photocatalytic membrane reactors (PMRs) in water treatment: Configurations and influencing factors. *Catalysts* **2017**, *7*, 224. [[CrossRef](#)]
16. Lee, A.; Libera, J.A.; Waldman, R.Z.; Ahmed, A.; Avila, J.R.; Elam, J.W.; Darling, S.B. Conformal nitrogen-doped TiO₂ photocatalytic coatings for sunlight-activated membranes. *Adv. Sustain. Syst.* **2017**, *1*, 1600041. [[CrossRef](#)]
17. Yang, K.; Li, X.; Yu, C.; Zeng, D.; Chen, F.; Zhang, K.; Huang, W.; Ji, H. Review on heterophase/homophase junctions for efficient photocatalysis: The case of phase transition construction. *Chin. J. Catal.* **2019**, *40*, 796–818. [[CrossRef](#)]
18. Rosman, N.; Salleh, W.N.W.; Razali, N.A.M. Heterojunction-based photocatalyst. In *Photocatalytic Systems by Design*; Elsevier: Amsterdam, The Netherlands, 2021; pp. 85–130.
19. Yang, F.; Yan, L.; Zhang, B.; He, X.; Li, Y.; Tang, Y.; Ma, C.; Li, Y. Fabrication of ternary NaTaO₃/g-C₃N₄/G heterojunction photocatalyst with enhanced activity for Rhodamine B degradation. *J. Alloys Compd.* **2019**, *805*, 802–810. [[CrossRef](#)]

20. Liang, H.; Guo, J.; Yu, M.; Zhou, Y.; Zhan, R.; Liu, C.; Niu, J. Porous loofah-sponge-like ternary heterojunction g-C₃N₄/Bi₂WO₆/MoS₂ for highly efficient photocatalytic degradation of sulfamethoxazole under visible-light irradiation. *Chemosphere* **2021**, *279*, 130552. [[CrossRef](#)] [[PubMed](#)]
21. Nasir, R.; Mukhtar, H.; Man, Z.; Mohshim, D.F. Material advancements in fabrication of mixed-matrix membranes. *Chem. Eng. Technol.* **2013**, *36*, 717–727. [[CrossRef](#)]
22. Bhol, P.; Yadav, S.; Altaee, A.; Saxena, M.; Misra, P.K.; Samal, A.K. Graphene-Based Membranes for Water and Wastewater Treatment: A Review. *ACS Appl. Nano Mater.* **2021**, *4*, 3274–3293. [[CrossRef](#)]
23. Jung, J.T.; Kim, J.F.; Wang, H.H.; Di Nicolo, E.; Drioli, E.; Lee, Y.M. Understanding the non-solvent induced phase separation (NIPS) effect during the fabrication of microporous PVDF membranes via thermally induced phase separation (TIPS). *J. Membr. Sci.* **2016**, *514*, 250–263. [[CrossRef](#)]
24. Jamalludin, M.R.; Harun, Z.; Hubadillah, S.K.; Basri, H.; Ismail, A.F.; Othman, M.H.D.; Shohur, M.F.; Yunos, M.Z. Antifouling polysulfone membranes blended with green SiO₂ from rice husk ash (RHA) for humic acid separation. *Chem. Eng. Res. Des.* **2016**, *114*, 268–279. [[CrossRef](#)]
25. Subramaniam, M.; Goh, P.; Lau, W.; Tan, Y.; Ng, B.; Ismail, A. Hydrophilic hollow fiber PVDF ultrafiltration membrane incorporated with titanate nanotubes for decolourization of aerobically-treated palm oil mill effluent. *Chem. Eng. J.* **2017**, *316*, 101–110. [[CrossRef](#)]
26. Rosman, N.; Salleh, W.N.W.; Mohamed, M.A.; Harun, Z.; Ismail, A.F.; Aziz, F. Constructing a compact heterojunction structure of Ag₂CO₃/Ag₂O in-situ intermediate phase transformation decorated on ZnO with superior photocatalytic degradation of ibuprofen. *Sep. Purif. Technol.* **2020**, 117391. [[CrossRef](#)]
27. Méricq, J.-P.; Mendret, J.; Brosillon, S.; Faur, C. High performance PVDF-TiO₂ membranes for water treatment. *Chem. Eng. Sci.* **2015**, *123*, 283–291. [[CrossRef](#)]
28. Sotto, A.; Boromand, A.; Zhang, R.; Luis, P.; Arsuaga, J.M.; Kim, J.; Van der Bruggen, B. Effect of nanoparticle aggregation at low concentrations of TiO₂ on the hydrophilicity, morphology, and fouling resistance of PES-TiO₂ membranes. *J. Colloid Interface Sci.* **2011**, *363*, 540–550. [[CrossRef](#)]
29. Kahrs, C.; Gühlstorf, T.; Schwellenbach, J. Influences of different preparation variables on polymeric membrane formation via nonsolvent induced phase separation. *J. Appl. Polym. Sci.* **2019**, 48852. [[CrossRef](#)]
30. Hořda, A.K.; Vankelecom, I.F. Understanding and guiding the phase inversion process for synthesis of solvent resistant nanofiltration membranes. *J. Appl. Polym. Sci.* **2015**, *132*. [[CrossRef](#)]
31. Liu, L.; Shen, F.; Zhang, B.; Jiang, H.; Li, J.; Luo, J.; Wu, H.; Khan, R.; Wan, Y. Fabrication of PES-based membranes with a high and stable desalination performance for membrane distillation. *RSC Adv.* **2016**, *6*, 107840–107850. [[CrossRef](#)]
32. Rahimpour, A.; Jahanshahi, M.; Mollahosseini, A.; Rajaeian, B. Structural and performance properties of UV-assisted TiO₂ deposited nano-composite PVDF/SPES membranes. *Desalination* **2012**, *285*, 31–38. [[CrossRef](#)]
33. Rizza, M.A.; Wijayanti, W.; Hamidi, N.; Wardana, I. Role of Intermolecular Forces on the Contact Angle of Vegetable Oil Droplets during the Cooling Process. *Sci. World J.* **2018**, *2018*. [[CrossRef](#)] [[PubMed](#)]
34. Vatanpour, V.; Madaeni, S.S.; Moradian, R.; Zinadini, S.; Astinchap, B. Fabrication and characterization of novel antifouling nanofiltration membrane prepared from oxidized multiwalled carbon nanotube/polyethersulfone nanocomposite. *J. Membr. Sci.* **2011**, *375*, 284–294. [[CrossRef](#)]
35. Zhang, D.; Dai, F.; Zhang, P.; Ana, Z.; Zhao, Y.; Chen, L. The photodegradation of methylene blue in water with PVDF/GO/ZnO composite membrane. *Mater. Sci. Eng. C* **2019**, *96*, 684–692. [[CrossRef](#)]
36. Salim, N.E.; Nor, N.; Jaafar, J.; Ismail, A.; Qtaishat, M.; Matsuura, T.; Othman, M.; Rahman, M.A.; Aziz, F.; Yusof, N. Effects of hydrophilic surface macromolecule modifier loading on PES/Og-C₃N₄ hybrid photocatalytic membrane for phenol removal. *Appl. Surf. Sci.* **2019**, *465*, 180–191. [[CrossRef](#)]
37. Ayyaru, S.; Dinh, T.T.L.; Ahn, Y.-H. Enhanced antifouling performance of PVDF ultrafiltration membrane by blending zinc oxide with support of graphene oxide nanoparticle. *Chemosphere* **2020**, *241*, 125068. [[CrossRef](#)]
38. Zinadini, S.; Rostami, S.; Vatanpour, V.; Jalilian, E. Preparation of antibiofouling polyethersulfone mixed matrix NF membrane using photocatalytic activity of ZnO/MWCNTs nanocomposite. *J. Membr. Sci.* **2017**, *529*, 133–141. [[CrossRef](#)]
39. Yu, L.Y.; Shen, H.M.; Xu, Z.L. PVDF-TiO₂ composite hollow fiber ultrafiltration membranes prepared by TiO₂ sol-gel method and blending method. *J. Appl. Polym. Sci.* **2009**, *113*, 1763–1772. [[CrossRef](#)]
40. Shukla, A.K.; Alam, J.; Alhoshan, M.; Dass, L.A.; Muthumareeswaran, M. Development of a nanocomposite ultrafiltration membrane based on polyphenylsulfone blended with graphene oxide. *Sci. Rep.* **2017**, *7*, 41976. [[CrossRef](#)] [[PubMed](#)]
41. Ma, Z.; Lu, X.; Wu, C.; Gao, Q.; Zhao, L.; Zhang, H.; Liu, Z. Functional surface modification of PVDF membrane for chemical pulse cleaning. *J. Membr. Sci.* **2017**, *524*, 389–399. [[CrossRef](#)]
42. Mahlangu, O.; Nackaerts, R.; Mamba, B.; Verliefde, A. Development of hydrophilic GO-ZnO/PES membranes for treatment of pharmaceutical wastewater. *Water Sci. Technol.* **2017**, *76*, 501–514. [[CrossRef](#)] [[PubMed](#)]
43. Bocchini, S.; Morlat-Thérias, S.; Gardette, J.-L.; Camino, G. Influence of nanodispersed boehmite on polypropylene photooxidation. *Polym. Degrad. Stab.* **2007**, *92*, 1847–1856. [[CrossRef](#)]
44. Qiu, S.; Wu, L.; Pan, X.; Zhang, L.; Chen, H.; Gao, C. Preparation and properties of functionalized carbon nanotube/PSF blend ultrafiltration membranes. *J. Membr. Sci.* **2009**, *342*, 165–172. [[CrossRef](#)]

45. Kim, S.; Park, C.M.; Jang, A.; Jang, M.; Hernández-Maldonado, A.J.; Yu, M.; Heo, J.; Yoon, Y. Removal of selected pharmaceuticals in an ultrafiltration-activated biochar hybrid system. *J. Membr. Sci.* **2019**, *570*, 77–84. [[CrossRef](#)]
46. Subramaniam, M.; Goh, P.; Lau, W.; Ng, B.; Ismail, A. AT-POME colour removal through photocatalytic submerged filtration using antifouling PVDF-TNT nanocomposite membrane. *Sep. Purif. Technol.* **2018**, *191*, 266–275. [[CrossRef](#)]
47. Liu, Y.; Shen, L.; Lin, H.; Yu, W.; Xu, Y.; Li, R.; Sun, T.; He, Y. A novel strategy based on magnetic field assisted preparation of magnetic and photocatalytic membranes with improved performance. *J. Membr. Sci.* **2020**, *612*, 118378. [[CrossRef](#)]
48. Castro-Muñoz, R.; Yáñez-Fernández, J.; Fila, V. Phenolic compounds recovered from agro-food by-products using membrane technologies: An overview. *Food Chem.* **2016**, *213*, 753–762. [[CrossRef](#)] [[PubMed](#)]
49. Galanakis, C.M. Separation of functional macromolecules and micromolecules: From ultrafiltration to the border of nanofiltration. *Trends Food Sci. Technol.* **2015**, *42*, 44–63. [[CrossRef](#)]
50. Park, G.-Y.; Lee, J.H.; Kim, I.S.; Cho, J. Pharmaceutical rejection by membranes for wastewater reclamation and reuse. *Water Sci. Technol.* **2004**, *50*, 239–244. [[CrossRef](#)]
51. Cho, H.-H.; Huang, H.; Schwab, K. Effects of solution chemistry on the adsorption of ibuprofen and triclosan onto carbon nanotubes. *Langmuir* **2011**, *27*, 12960–12967. [[CrossRef](#)] [[PubMed](#)]
52. Singh, R.; Yadav, V.; Purkait, M.K. Cu₂O photocatalyst modified antifouling polysulfone mixed matrix membrane for ultrafiltration of protein and visible light driven photocatalytic pharmaceutical removal. *Sep. Purif. Technol.* **2019**, *212*, 191–204. [[CrossRef](#)]
53. Oyetade, O.A.; Martincigh, B.S.; Skelton, A.A. Interplay between electrostatic and hydrophobic interactions in the pH-dependent adsorption of ibuprofen onto acid-functionalized multiwalled carbon nanotubes. *J. Phys. Chem. C* **2018**, *122*, 22556–22568. [[CrossRef](#)]
54. Mahmoudi, E.; Ng, L.Y.; Ang, W.L.; Chung, Y.T.; Rohani, R.; Mohammad, A.W. Enhancing morphology and separation performance of polyamide 6, 6 membranes by minimal incorporation of silver decorated graphene oxide nanoparticles. *Sci. Rep.* **2019**, *9*, 1216. [[CrossRef](#)] [[PubMed](#)]
55. Moustakas, N.; Katsaros, F.; Kontos, A.; Romanos, G.E.; Dionysiou, D.; Falaras, P. Visible light active TiO₂ photocatalytic filtration membranes with improved permeability and low energy consumption. *Catal. Today* **2014**, *224*, 56–69. [[CrossRef](#)]
56. Albiter, E.; Valenzuela, M.; Alfaro, S.; Valverde-Aguilar, G.; Martínez-Pallares, F. Photocatalytic deposition of Ag nanoparticles on TiO₂: Metal precursor effect on the structural and photoactivity properties. *J. Saudi Chem. Soc.* **2015**, *19*, 563–573. [[CrossRef](#)]
57. Mino, L.; Pellegrino, F.; Rades, S.; Radnik, J.R.; Hodoroaba, V.-D.; Spoto, G.; Maurino, V.; Martra, G. Beyond shape engineering of TiO₂ nanoparticles: Post-synthesis treatment dependence of surface hydration, hydroxylation, Lewis acidity and photocatalytic activity of TiO₂ anatase nanoparticles with dominant {001} or {101} facets. *ACS Appl. Nano Mater.* **2018**, *1*, 5355–5365. [[CrossRef](#)]
58. Pan, L.; Zou, J.-J.; Zhang, X.; Wang, L. Water-mediated promotion of dye sensitization of TiO₂ under visible light. *J. Am. Chem. Soc.* **2011**, *133*, 10000–10002. [[CrossRef](#)] [[PubMed](#)]
59. Higashimoto, S.; Okada, K.; Morisugi, T.; Azuma, M.; Ohue, H.; Kim, T.-H.; Matsuoka, M.; Anpo, M. Effect of surface treatment on the selective photocatalytic oxidation of benzyl alcohol into benzaldehyde by O₂ on TiO₂ under visible light. *Top. Catal.* **2010**, *53*, 578–583. [[CrossRef](#)]
60. Wu, H.; Fu, Q.; Li, Y.; Cui, Y.; Wang, R.; Su, N.; Lin, L.; Dong, A.; Ning, Y.; Yang, F. Controlled growth of uniform two-dimensional ZnO overlayers on Au (111) and surface hydroxylation. *Nano Res.* **2019**, *12*, 2348–2354. [[CrossRef](#)]
61. Newberg, J.T.; Goodwin, C.; Arble, C.; Khalifa, Y.; Boscoboinik, J.A.; Rani, S. ZnO (1010) surface Hydroxylation under ambient water vapor. *J. Phys. Chem. B* **2018**, *122*, 472–478. [[CrossRef](#)]
62. Wang, M.; Yang, G.; Jin, P.; Tang, H.; Wang, H.; Chen, Y. Highly hydrophilic poly (vinylidene fluoride)/meso-titania hybrid mesoporous membrane for photocatalytic membrane reactor in water. *Sci. Rep.* **2016**, *6*, 19148. [[CrossRef](#)] [[PubMed](#)]
63. Rosman, N.; Salleh, W.N.W.; Razali, N.A.M.; Ahmad, S.Z.N.; Ismail, N.H.; Aziz, F.; Harun, Z.; Ismail, A.F.; Yusof, N. Ibuprofen removal through photocatalytic filtration using antifouling PVDF-ZnO/Ag₂CO₃/Ag₂O nanocomposite membrane. *Mater. Today Proc.* **2021**, *42*, 69–74. [[CrossRef](#)]